



# Corrosion Inhibition of AZ31-xLi ( $x = 4, 8, 12$ ) magnesium alloys in sodium chloride solutions by aqueous molybdate<sup>☆</sup>

Maria A. Osipenko<sup>a</sup>, Andrei V. Paspelau<sup>a</sup>, Aliaksandr A. Kasach<sup>b</sup>, Jacek Ryl<sup>c,\*</sup>,  
Konrad Skowron<sup>d,e</sup>, Janusz Adamiec<sup>f</sup>, Irina I. Kurilo<sup>a</sup>, Dzmitry S. Kharytonau<sup>d,e,\*\*,1</sup>

<sup>a</sup> Department of Physical, Colloid, and Analytical Chemistry, Belarusian State Technological University, Minsk 220006, Belarus

<sup>b</sup> Department of Chemistry, Electrochemical Production Technology, and Materials for Electronic Equipment, Belarusian State Technological University, Minsk 220006, Belarus

<sup>c</sup> Advanced Materials Center and Institute of Nanotechnology and Materials Engineering, Gdańsk University of Technology, Gdańsk 80-233, Poland

<sup>d</sup> Electrochemistry and Corrosion Laboratory, Jerzy Haber Institute of Catalysis and Surface Chemistry, Polish Academy of Sciences, Krakow 30-239, Poland

<sup>e</sup> Soft Matter Nanostructures, Jerzy Haber Institute of Catalysis and Surface Chemistry, Polish Academy of Sciences, Krakow 30-239, Poland

<sup>f</sup> Institute of Materials Science, Silesian University of Technology, Katowice 40-019, Poland

## ARTICLE INFO

### Keywords:

Magnesium-lithium alloy  
Dynamic electrochemical impedance spectroscopy  
Corrosion mechanism  
Molybdate inhibitor  
Inhibitor efficiency

## ABSTRACT

Corrosion of lithium-containing AZ31 magnesium alloys AZ31-xLi ( $x = 4, 8, \text{ and } 12 \text{ wt\%}$ ) has been examined in 0.05 M NaCl solution with and without 10–150 mM of Na<sub>2</sub>MoO<sub>4</sub> inhibitor. Potentiodynamic polarization, electrochemical impedance spectroscopy (EIS), and dynamic electrochemical impedance spectroscopy (DEIS) measurements were used to correlate the phase composition and microstructure of the alloys with their corrosion propensity and effectiveness of the molybdate inhibitor, giving high inhibition efficiency (>85%) at concentrations higher than ca. 35 mM. Post-corrosion microstructure, Raman, and X-ray photoelectron spectroscopy analyses allowed to provide the inhibition mechanism of AZ31-xLi alloys by molybdate ions.

## 1. Introduction

Magnesium and its alloys are attractive and promising materials for the aerospace, automotive, and medical industries due to their low density, excellent formability, non-toxicity, and damping properties [1–4]. However, unlike aluminum and titanium, Mg alloys are characterized by a low corrosion resistance due to their extreme reactivity and the absence of a stable oxide layer [5–8]. At present, the main ways of tailoring corrosion and mechanical properties of magnesium alloys are alloying, surface modification, as well as the use of corrosion inhibitors [2,9–11].

There are several groups of Mg alloys, which are extensively used in industry. Among them most common are Mg-Al-Zn, Mg-Ca, and Mg-REEs (rare-earth elements) alloys [6,7,12]. The AZ-series Mg-Al-Zn alloys account for more than 90% of currently used magnesium alloys [13]. Alloying with aluminum improves the strength, hardness, casting

properties, and corrosion resistance of magnesium alloys [2,14]. The microstructure of such alloys is a solid solution of aluminum and  $\beta$ -phase (Mg<sub>17</sub>Al<sub>12</sub>) in Mg, the presence of which increases the corrosion potential and reduces its corrosion rate.

Continuous technological development and search for new energy-saving technologies have promoted further development of ultralight and superplastic structural materials [15–17]. Among them, magnesium-lithium (Mg-Li) alloys are the lightest metal engineering materials [16,18]. The binary phase diagram of the Mg-Li system shows [19,20], that alloying of magnesium with lithium increases the ductility of the alloy due to the transformation of the crystal structure from a hexagonal close-packed (hcp) with a lithium content of less than 5.7 wt% ( $\alpha$ -phase is a solid solution of lithium in magnesium) to body-centered cubic (bcc) with a lithium content of more than 11.3 wt% ( $\beta$ -phase, a solid solution of magnesium in lithium). In turn, magnesium alloys containing 5.7–11.3 wt% of Li have both hcp and bcc crystal structures

<sup>☆</sup> Preprint of this manuscript is available at: <https://chemrxiv.org/engage/chemrxiv/article-details/65fc0a5166c138172975afd1> (<https://doi.org/10.26434/chemrxiv-2024-k1lr3>)

\* Corresponding author.

\*\* Correspondence to: Jerzy Haber Institute of Catalysis and Surface Chemistry, Polish Academy of Sciences, Poland.

E-mail addresses: [jacek.ryl@pg.edu.pl](mailto:jacek.ryl@pg.edu.pl) (J. Ryl), [dmitry.kharitonov@ikifp.edu.pl](mailto:dmitry.kharitonov@ikifp.edu.pl) (D.S. Kharytonau).

<sup>1</sup> ORCID: 0000-0003-2071-3975

[16,21,22]. Due to the simultaneous presence of the  $\alpha$ - and  $\beta$ -phases, such magnesium alloys are characterized by medium strength and high ductility [20]. This difference in the microstructure of the alloys has a significant influence on the corrosion rate of Mg-Li alloys. Xu et al. [18] and Li et al. [23] reported that Mg-Li alloys containing high amounts of Li (above 10.3 wt%) have superior corrosion resistance due to the formation of a protective lithium carbonate surface film upon bcc Mg-Li matrix. However, Zhao et al. [24] for Mg-4Li and Mg-12Li alloys reported opposite corrosion behavior and increased corrosion rates. To improve the industrial applicability of such alloys, it is possible to add additional alloying elements to their composition. Meanwhile, the inclusion of small amounts of Al to binary Mg-Li alloys improves their mechanical properties, while maintaining the ultra-low density of these alloys to a considerable degree [17,25,26].

The influence of the lithium amount on the corrosion resistance of Mg alloys, with Al, Zn, Nd, and other alloying elements is not so straightforward [16,27–33]. Common Mg alloys have various types of intermetallic particles (IMPs) in their microstructure, most of them being cathodic relative to the alloy matrix [16,34,35]. The corrosion rate of Mg-Li alloys with low Li content is comparable to that of traditional Mg alloys without Li [16]. The addition of a high amount of Li causes the formation of new types of Li-rich IMPs, commonly Mg-Li and Al-Li types [36], intensifying local galvanic corrosion of such alloys [16, 37]. An increase in the volume fraction of the Li-containing IMPs promotes filiform corrosion along the grain boundaries and inside the  $\beta$ -Li phase [38]. An increase in the corrosion rate with increasing amounts of Li was reported for Mg-Al-Li, Mg-Li-Ca, Mg-Li-Al-Zn-Y, Mg-Zn-Li, and Mg-Al-Li-Zn alloys [27,29,31,39]. However, corrosion and possible inhibition mechanisms of such alloys still require deeper studies and understanding. It is known that lithium salts can be used as effective corrosion inhibitors for Mg alloys due to the formation of a surface  $\text{Li}_2\text{CO}_3$  film [40], while the knowledge on the use of inhibitors for corrosion protection of Mg-Li alloys is very limited. Nevertheless, the implementation of an effective inhibitor can significantly improve the corrosion resistance of Mg-Li alloys and extend their applications.

There are numerous potential corrosion inhibitors for magnesium alloys [10]. Among them, inorganic compounds usually act as precipitation-type inhibitors, and their effectiveness is strongly related to the microstructure of the examined alloy since the inhibition is usually based on retardation of the cathodic activity of second-phase precipitates [41–43]. In our previous works [34,44,45], we have shown that inorganic oxidizing anions, such as permanganates and molybdates, are effective inhibitors for the corrosion protection of AZ31 and WE43 alloys. Examination of the AZ31 alloy revealed that the inhibition mechanism is based on the formation of a surface oxide layer suppressing the cathodic activity of IMPs and the anodic activity of the Mg matrix. However, Lamaka et al. [43] in their comprehensive screening of corrosion inhibitors for Mg alloys specifically underlined that the majority of corrosion inhibitors of Mg alloys are not universal and their inhibiting efficiency strongly depends on the type and amount of alloying elements in the alloy. This is also confirmed by our previous studies [34,44,45]. At the same time, the inhibiting efficiency provided by many inhibitors, including inorganic ones, depends on their concentration in the examined media [34,43,45]. Therefore, investigation of the inhibition mechanisms of Mg-Al-Li alloys depending on the amount of Li and concentration of the inhibitor is of significant importance to speed up the implementation of such alloys and inhibitors into commercial usage.

Recently, special attention has been paid to the examination of the surface films formed on Li-containing Mg alloys. Mapping the Li distribution in Mg-Li alloys is a challenging but essential task for understanding the origin of corrosion resistance in this class of Mg alloys [15, 33,46–48]. On the other hand, the accurate examination of corrosion processes of Mg alloys, especially by electrochemical techniques, is still important. In our recent studies [49,50] we have proposed a new approach to implement multisine dynamic electrochemical impedance

spectroscopy (DEIS) monitoring as an expedient method to examine the kinetics of the nonstationary corrosion process of Mg alloys. We believe that this technique also can be effectively used to monitor the inhibition effectiveness of corrosion inhibitors towards Mg alloys [50], as was previously done for Al alloys [51–53]. To our best knowledge, evaluation of corrosion processes of Mg alloys containing Li, in particular, AZ31-xLi ( $x = 4, 8, 12$ ) alloys by dynamic multisine DEIS approach and their corrosion protection by soluble molybdates have not been described in the literature. Moreover, it is important to establish the correlation of the protection mechanism with the amount of Li and, consequently, the microstructure of these alloys.

The aim of the present study was to elucidate the inhibition efficiency of molybdate ions towards the AZ31-xLi ( $x = 4, 8, 12$ ) Mg alloys depending on the amount of the molybdate inhibitor in the corrosive medium and Li in the AZ31 Mg alloy. To do so, a set of classical electrochemical techniques, coupled with DEIS monitoring and spectroscopic surface analyses, has been used and the inhibition mechanism of AZ31-xLi ( $x = 4, 8, 12$ ) Mg alloys by soluble molybdates has been proposed. A detailed examination of corrosion processes and inhibition efficiency of molybdates towards the AZ31 alloy without Li addition has been reported in our previous publication [44]. Therefore, this alloy is not examined in the present contribution, and data from [44] can be used as a reference.

## 2. Experimental

### 2.1. Materials and sample preparation

Magnesium alloys AZ31-xLi ( $x = 4, 8, 12$ ) examined in this study were obtained by a casting method. The target elemental composition of the alloys was as that of the AZ31 alloy with the addition of 4, 8, or 12 wt % of Li. Metals used for the process were purchased from Sigma Aldrich. The process was carried out in a Balzers VSG 02 single-chamber vacuum induction melting furnace at a temperature of 650°C, and a pressure of 600 Torr ( $8 \times 10^4$  Pa) in the argon atmosphere. Obtained billets were then cut into samples with sizes ca. 20 mm  $\times$  20 mm  $\times$  5 mm. The samples were ground up to P4000 grit emery paper in 99.9% ethanol before every corrosion and surface investigation experiment. After grinding, the samples were cleaned for 5 min in a Skymen JP-008 ultrasonic bath in 99.9% ethanol.

The density of the obtained alloys was determined by the hydrostatic weighing method at 27.5°C utilizing acetone as a liquid medium (to avoid degradation of alloys during the measurement) and analytical balance with 0.0001 g accuracy.

### 2.2. Surface analysis

The X-ray diffraction (XRD) analysis of the obtained alloys was performed using a PANalytical X'Pert Pro diffractometer operating with a Ni-filtered  $\text{Cu K}\alpha$  (1.5406 Å) radiation. XRD patterns were registered in the  $2\theta$  range of 20–90° with a scan rate of 1.5°/min.

A Hitachi SU8000 and a JEOL JSM-5610 LV scanning electron microscopes (SEM) were used to examine the surface morphology of the alloys before and after corrosion experiments. The elemental composition was investigated using an energy-dispersive X-ray spectroscopy (EDX) detector of the used SEMs.

Raman spectra of the AZ31-xLi alloys' surface were acquired after corrosion experiments with a Jobin-Yvon T64000 Raman spectroscopy system. The system is equipped with a green 514.5 nm Ar laser with an incident power of ca. 5 mW. The total acquisition time of one spectrum was 240 s.

The optical top-surface images of the alloys after corrosion experiments were acquired on a Keyence VHX-7000 high-accuracy 4 K digital microscope.

The X-ray photoelectron spectroscopy (XPS) spectra were obtained directly after exposure of the examined alloys to the 0.05 M sodium

chloride solutions additionally containing 150 mM of the molybdate inhibitor for 1 h. A ThermoFisher Scientific Escalab 250Xi spectrometer was used. The measurement procedure was similar to our previous publications [34,44]. Measurements were performed with an Al K $\alpha$  source at a pass energy of 10 eV. Before XPS measurements, samples were thoroughly rinsed with deionized water, dried in a flow of nitrogen in an ambient atmosphere, and immediately transferred to the spectrometer chamber. For the analysis of the spectra, correction of the carbon C 1 s excitation (284.6 eV) charge was performed.

### 2.3. Corrosion measurements

Corrosion studies were performed in solutions prepared with NaCl ( $\geq 99.5$ ) and Na<sub>2</sub>MoO<sub>4</sub>  $\times$  2 H<sub>2</sub>O ( $\geq 99.5$ ) received from Chemsolute (Th. Geyer Polska). As a reference corrosion medium, 0.05 M NaCl solution was selected. Utilization of this medium prevents rapid degradation of Mg alloys and was previously used in our studies of inorganic corrosion inhibitors of Mg and Al alloys [34,44,45,54]. The effectiveness of the inhibition was examined in the range of 10–150 mM of Na<sub>2</sub>MoO<sub>4</sub> in the examined 0.05 M NaCl solution.

Classical electrochemical experiments were performed on an Autolab PGSTAT302N potentiostat/galvanostat with an FRA32M module for electrochemical impedance spectroscopy (EIS) measurements. One series of measurements included monitoring of the open-circuit potential (OCP) for 1000 s, registration of the EIS spectrum, determination of polarization resistance by low-amplitude cyclic voltammetry (CV), and potentiodynamic polarization scan. A three-electrode electrochemical cell consisted of a Pt counter electrode (mesh), reference electrode (sat. Ag/AgCl), and examined Mg alloy as a working electrode.

The classical EIS measurements were carried out at the OCP over a frequency range from 10<sup>5</sup> to 10<sup>-2</sup> Hz. A sinusoidal perturbation amplitude of 10 mV was used. The ZView 3.2c software was used for data analysis and spectra fitting.

The polarization resistance ( $R_p$ ) of the samples was calculated from the slope of CV measurement curves in the overpotential range of  $\pm 10$  mV vs. the OCP. The values of  $R_p$  were calculated as:

$$R_p = \Delta E / \Delta i_{\Delta E \rightarrow 0}, \quad (1)$$

Potentiodynamic polarization curves were recorded at a scan rate of 1.0 mV/s in a potential window from -300 mV to +300 mV vs. the OCP.

The inhibition efficiency,  $IE$ , of the sodium molybdate inhibitor was calculated based on the results of electrochemical measurements using the following formulas:

$$IE, \% = \frac{R - R^0}{R} 100\%, \quad (2)$$

$$IE, \% = \frac{i_{\text{corr}}^0 - i_{\text{corr}}}{i_{\text{corr}}^0} 100\%, \quad (3)$$

where  $R^0$ ,  $i_{\text{corr}}^0$ ,  $R$ , and  $i_{\text{corr}}$  are resistances and corrosion current densities in the absence and presence of the inhibitor, respectively.

The multisine dynamic electrochemical impedance spectroscopy (DEIS) monitoring was performed using a two-channel Biologic SP-300 potentiostat connected to a PXI-4464 AC measurement card and a PXI-6124 AC/DC signal module. Following the limitation on the high-frequency limit of the used measurement card, spectra were recorded in a narrower frequency range of 22 kHz–0.7 Hz with 10 points per frequency decade. To evaluate the inhibition effectiveness of the molybdate inhibitor as a function of its concentration, a Lead Fluid peristaltic micropump was used. In this case, during the first 600 s of the experiment, DEIS spectra were recorded in a 0.05 M NaCl solution without the inhibitor. After this, the concentrated solution of the molybdate inhibitor was gradually introduced into the measured system by the peristaltic pump for 3000 s to achieve the final concentration of the inhibitor in the examined solution of 150 mM. The measurement

was then continued for 600 s in conditions with 150 mM of the sodium molybdate inhibitor (Fig. S1 in Supplementary Information). Further details on the experimental setup and the measurement conditions are reported elsewhere [51]. The fitting of the obtained impedance spectra was performed based on the Nelder-Mead algorithm [55].

All corrosion measurements reported in this contribution were at least duplicated and a new sample was used to perform each series of measurements.

## 3. Results and discussion

### 3.1. Microstructure characterization

The results of the XRD analysis of obtained AZ31-xLi alloys are shown in Fig. 1. The obtained data indicate that the AZ31-4Li mostly consists of an HCP structured  $\alpha$ -Mg phase ( $\alpha$ -Mg, ICDD card #01-079-6692). An increase in the amount of lithium in the alloy leads to a shift of  $\alpha$ -Mg reflexes to larger  $2\theta$  [23], and the occurrence of the reflexes corresponding to a BCC  $\beta$ -Li phase (ICDD card #04-006-5779), which is the main phase in the AZ31-12Li alloy. XRD patterns of all alloys also have low-intensity reflexes at  $2\theta$  ca. 23 and 40°. The AZ-series Mg alloys usually have Mg-Al, Al-Mn, and Al-Mn-Zn IMPs [44,56]. Recently, Zhang et al. [15] confirmed by electron energy-loss spectroscopy that Al-containing IMPs in Mg-Li-Al alloys are in fact rich in Li. Therefore, these reflexes were assigned to the Al-Li phases (ICDD card #00-003-1215) [15,20,57]. The results of the measurements by the hydrostatic weighing revealed the density values of  $1.78 \pm 0.01$ ,  $1.57 \pm 0.03$ , and  $1.47 \pm 0.02$  g/cm<sup>3</sup> for AZ31-4Li, AZ31-8Li, and AZ31-12Li alloys, respectively. These values are comparable with the literature data for Mg-Li-Al alloys [17,25,33].

Fig. 2 shows the surface microstructure of as-polished AZ31-xLi alloys, examined by SEM. The amount of Li determines the type and distribution of phases in the microstructure of the obtained alloys. The direct use of the EDX analysis for the detection of lithium and examination of its surface distribution is not possible as more advanced techniques should be used [15]. Therefore, in the qualitative analysis of the microstructure of the AZ31-xLi alloys, the phase assignments between  $\alpha$ -Mg and  $\beta$ -Li were provisionally made based on the possibilities of the electron backscattering mode of the SEM. In this case, the lighter areas correspond to elements with a higher atomic number ( $\alpha$ -Mg), and the darker areas correspond to elements with a lower atomic number ( $\beta$ -Li) [38]. While this approach is not so straightforward, it is often used to distinguish between these two phases [38,58–60]. These phases were also identified by the measurement of the surface Volta potential distribution maps (not shown in the present contribution).

The principal constituents of the AZ31-4Li alloy are IMPs distributed in the  $\alpha$ -Mg alloy matrix (Fig. 2a). These IMP phases were rather small (usually less than 10  $\mu$ m). In the case of the AZ31-8Li alloy (Fig. 2b), two

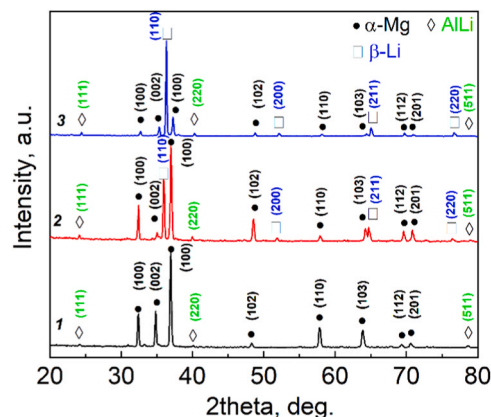
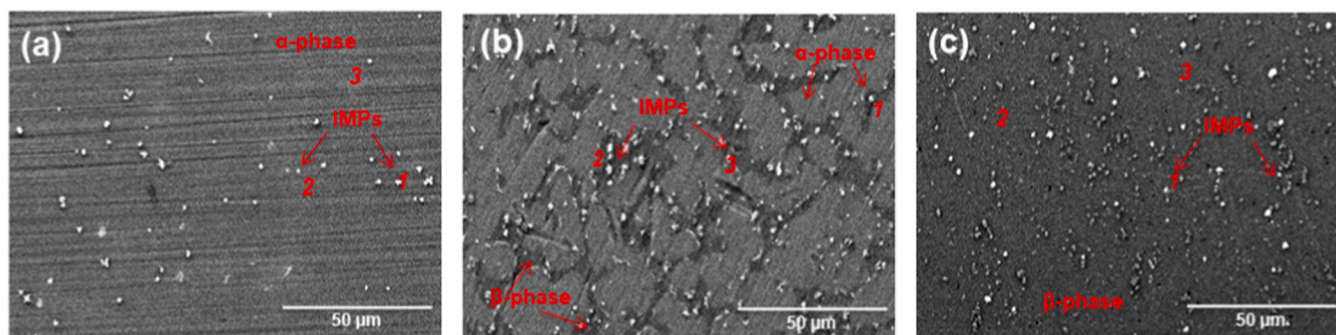


Fig. 1. XRD patterns of (1) AZ31-4Li, (2) AZ31-8Li, and (3) AZ31-12Li alloys.



**Fig. 2.** SEM images in backscatter mode of (a) AZ31-4Li, (b) AZ31-8Li, and (c) AZ31-12Li alloys. In each panel, areas marked with numbers correspond to points of EDX analysis listed in Table 1.

main phases  $\alpha$ -Mg (lighter regions) and  $\beta$ -Li (darker regions) with increased number of IMPs. The AZ31-12Li alloy (Fig. 2c) mostly contains the  $\beta$ -Li phase with a further increased number of IMPs. The observed microstructures also support the results of the XRD analysis (Fig. 1) and the formation of Al-Li-type IMPs in these Mg alloys.

The quantitative EDX analysis of the characteristic surface constituents (Fig. 2, Table 1) revealed the presence of Mg-Al, Al-Mn, and Al-Zn IMPs in the microstructure of the AZ31-xLi alloys. The elemental distribution maps (Fig. 3) also confirmed the formation of IMPs in the microstructure. For the AZ31-4Li and AZ31-12Li, Al-Mn-type IMPs are formed in the microstructure, while in the microstructure of AZ31-8Li, there are regions rich in Al, which suggests the presence of Al-Mg IMPs. At the same time, the formation of Li-rich IMPs in these alloys is also possible. The precipitation of Al-Li phases is thermodynamically favorable compared to Al-Mg phases, which is due to a larger difference in electronegativity of Al and Li (0.63) compared to Al and Mg (0.30). The difference between the relative electronegativity between Mg and Mn is 0.24. Therefore, the formation of Mg-Al IMPs is more expected than Mg-Mn, which is also supported by the XRD data [12].

### 3.2. Corrosion analysis

#### 3.2.1. Evolution of pH and OCP at initial stages of corrosion in chloride-containing solutions

The dynamics of changes in the pH and OCP of the examined alloys in 0.05 M sodium chloride solutions with different amounts of the sodium molybdate inhibitor are shown in Fig. 4. In each condition, both parameters were followed for 1000 s. The initial value of the pH of the as-prepared sodium chloride solution was around 6.7. In this media, a pronounced increase in the bulk pH with time was observed with an increase in the amount of Li in the alloys. This trend can be associated with the initiation of the corrosion process and the tendency of the alloy to corrode [61]. After 1000 s of exposure of AZ31-4Li, AZ31-8Li, and AZ31-12Li to the 0.05 M NaCl solution without the inhibitor, the pH values increased to 7.2, 7.7, and 9.2, respectively (Fig. 4a-c). The introduction of  $\text{Na}_2\text{MoO}_4$  into the 0.05 M NaCl solution increased the

**Table 1**  
EDX elemental analysis of as-polished AZ31-xLi alloys.

Conditions	Area	Elemental composition, at%			
		Mg	Al	Zn	Mn
AZ31-4Li (Fig. 2a)	1	37.1	35.0	0.5	27.4
	2	33.2	38.5	0.5	27.8
	3	99.0	1.0	-	-
AZ31-8Li (Fig. 2b)	1	79.3	18.8	1.9	-
	2	93.1	5.0	0.1	1.7
	3	97.7	2.0	-	0.3
AZ31-12Li (Fig. 2c)	1	9.0	31.7	0.4	58.9
	2	98.3	1.5	0.2	-
	3	96.7	2.6	0.8	-

initial pH of the solution because molybdic acid is a weak acid ( $\text{pK}_a = 6$ ) and its salts are hydrolyzed in aqueous solutions. The pH value was rapidly increasing in the presence of 10 and 50 mM of the molybdate inhibitor, suggesting activation of the corrosion process in time. In turn, at higher concentrations of the molybdate in the solution pH remained quite stable in time, which is a sign of improved corrosion resistance and retardation of the corrosion process.

The OCP profiles (Fig. 4d-f) showed similar tendencies. The lowest values of the OCP were observed in the 0.05 M NaCl solution without the inhibitor. The initial values of the OCP in the presence of the molybdate inhibitor were higher for all alloys, suggesting rapid adsorption of molybdate ions on the surface and the retardation of the anodic process [34]. At low concentrations of the inhibitor (10 mM), some small but distinct potential fluctuations were observed for the AZ31-8Li sample, which might be a sign of a less stable surface film and local corrosion attack. The values of the stabilized OCP increased with higher concentrations of the added molybdate inhibitor in the solution. The shape of the obtained OCP dependencies suggests that at high concentrations, molybdate ions are rapidly adsorbed on the surface and form a surface film over all examined alloys, which results in an increase of the electrode potential and its shift in the noble direction.

#### 3.2.2. Potentiodynamic polarization

Fig. 5 summarizes the results of the potentiodynamic polarization measurements of AZ31-xLi alloys in examined solutions. To assign the values of the corrosion current density it is important to consider that kinetics of anodic processes in the case of Mg alloys is not fully controlled by the charge transfer. In the examined case, it will be significantly affected by the formed oxide/hydroxide film or Mo-rich protective film of the inhibitor at low overpotentials or IR-drop through the electrolyte at high overpotentials. Hence, the values of the corrosion current density ( $i_{\text{corr}}$ ) were calculated by the extrapolation of only the cathodic slope of the polarization curve back to the corrosion potential ( $E_{\text{corr}}$ ). In the absence of the inhibitor, high corrosion rates of all investigated alloys were observed. In chloride media, polarization curves showed no sign of surface passivation. A higher content of lithium in the alloy resulted in a shift of  $E_{\text{corr}}$  to more noble values. However, the values of  $i_{\text{corr}}$  increased significantly (Table 2) and were  $(2.09 \pm 0.32) \times 10^{-5}$ ,  $(7.08 \pm 0.81) \times 10^{-5}$ , and  $(1.47 \pm 0.9) \times 10^{-4}$  A/cm<sup>2</sup> for AZ31-4Li, AZ31-8Li and AZ31-12Li alloys, respectively. Interestingly, an increase in  $E_{\text{corr}}$  values is usually associated with the retardation of anodic kinetics and improved corrosion resistance. However, in this case, it was followed with an almost an order of magnitude increase in the  $i_{\text{corr}}$  values. This inconsistency can be explained by the increase in cathodic current with the increased amount of Li in the alloy and the so-called cathodic activation phenomenon, observed in the course of corrosion of Mg alloys [23,62,63].

In 0.05 M NaCl solutions containing the molybdate inhibitor polarization dependencies revealed a significant change in the kinetics of the anodic and cathodic processes. The values of the corrosion potential in

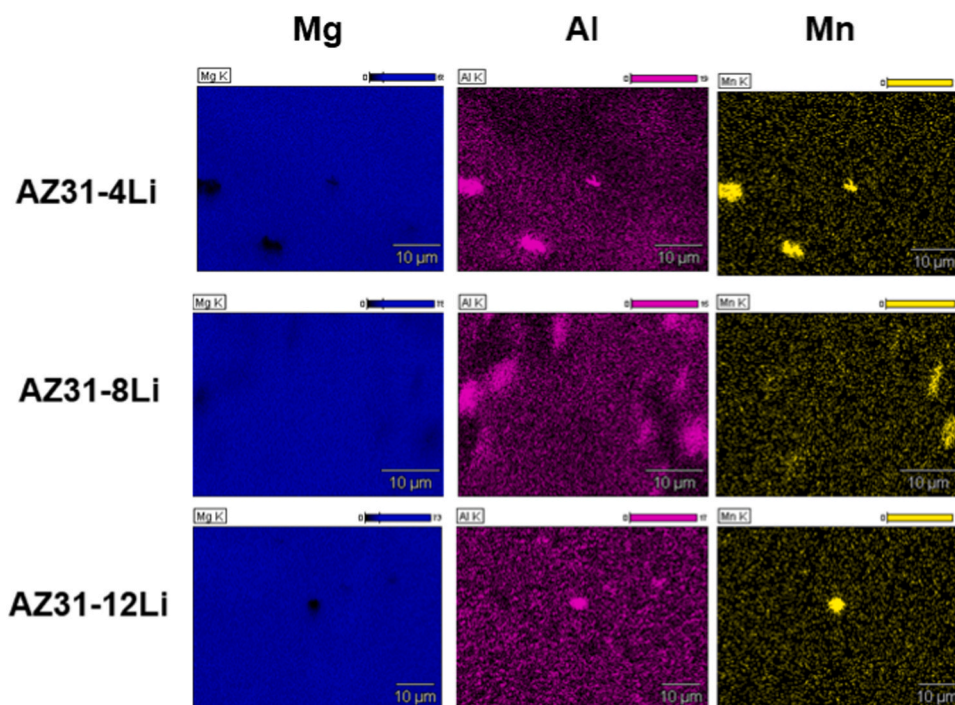


Fig. 3. EDX maps showing the elemental distribution of Mg (to the left), Al (in the middle), and Mn (to the right) over the surface of as-polished AZ31-xLi alloys.

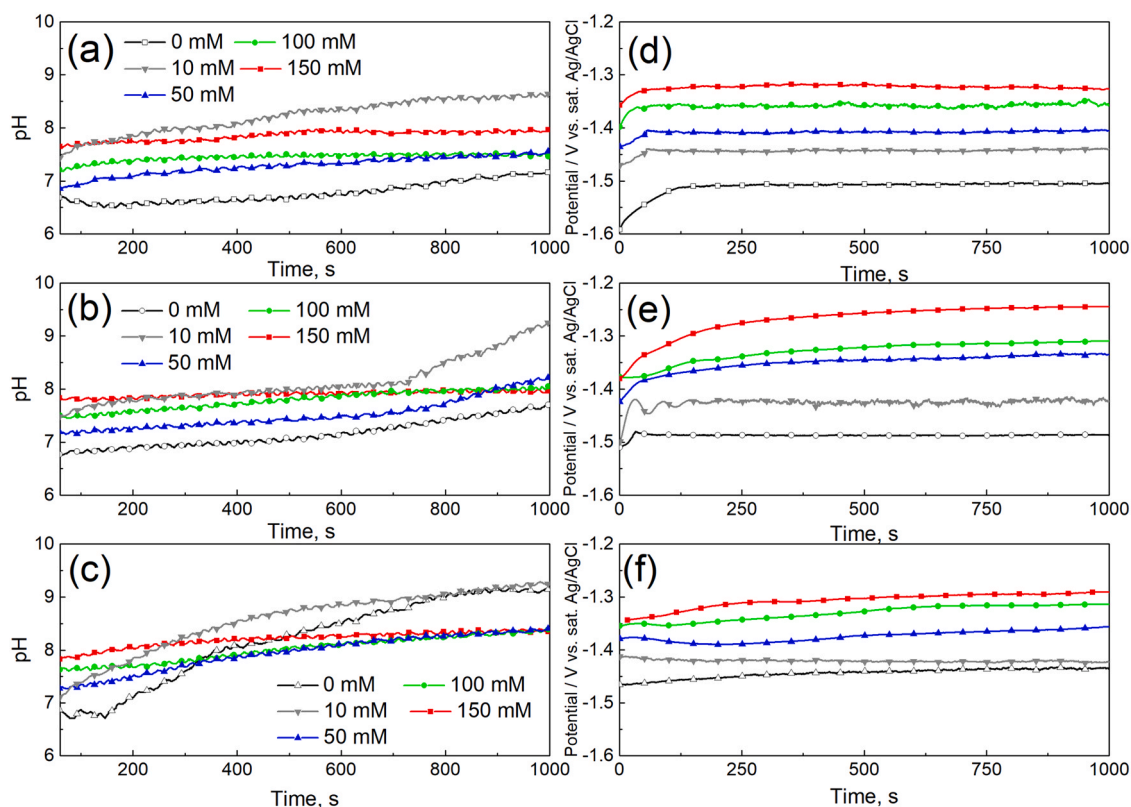


Fig. 4. Evolution of pH (a–c) and OCP (d–f) profiles in time of AZ31–4Li (a, d), AZ31–8Li (b, e), and AZ31–12Li (c, f) in 0.05 M NaCl solution with and without the  $\text{Na}_2\text{MoO}_4$  inhibitor. Legend in panels to the left also corresponds to panels to the right.

the presence of the molybdate inhibitor were shifted towards more noble values. This shift was larger as the concentration of the inhibitor in the solution increased and, in this case, was directly associated with the interaction of the molybdate inhibitor with the surface of the alloys and

retardation of the corrosion kinetics. The maximum difference between  $E_{\text{corr}}$  in the inhibited and reference solutions decreased as the amount of Li in the alloy increased and was ca. 140, 100, and 65 mV for AZ31–4Li, AZ31–8Li, and AZ31–12Li alloys, respectively. Furthermore, at the

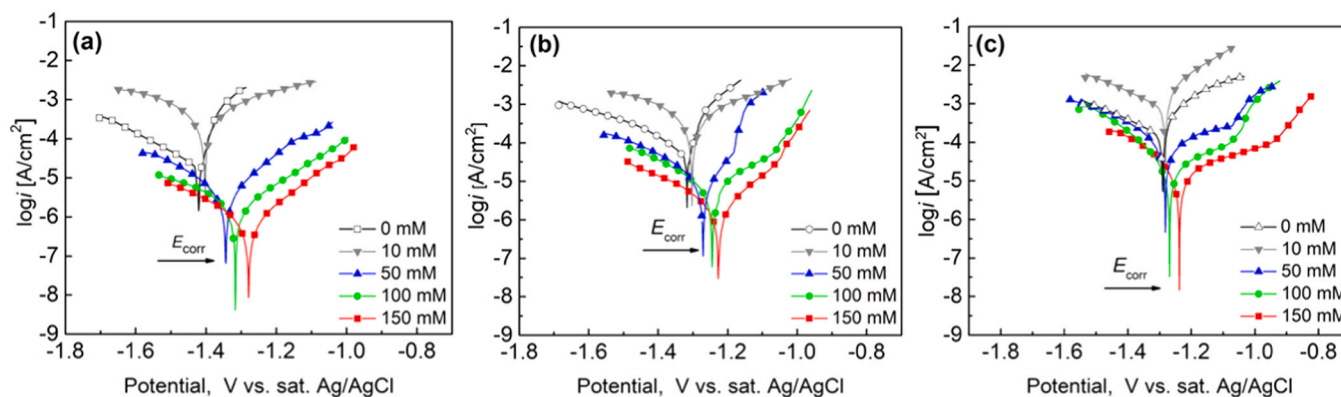


Fig. 5. Potentiodynamic polarization curves of AZ31–4Li (a), AZ31–8Li (b), and AZ31–12Li (c) in 0.05 M NaCl without and with varying amounts of  $\text{Na}_2\text{MoO}_4$ . The scan rate is 1 mV/s and scanning was done from the cathodic to the anodic side.

Table 2

Parameters obtained from the analysis of potentiodynamic polarization curves.

Concentration of inhibitor, mM	$i_{\text{corr}}$ , $\text{A cm}^{-2}$	$E_{\text{corr}}$ , V	IE, %	$i_{\text{a}}$ , $\text{A cm}^{-2}$ (at $-1.10$ V)	$i_{\text{c}}$ , $\text{A cm}^{-2}$ (at $-1.45$ V)
AZ31–4Li					
0	$(2.09 \pm 0.32) \times 10^{-5}$	$-1.411 \pm 0.010$	–	–	$2.99 \times 10^{-5}$
10	$(1.94 \pm 0.92) \times 10^{-4}$	$-1.394 \pm 0.034$	–	$2.53 \times 10^{-3}$	$5.38 \times 10^{-4}$
50	$(4.35 \pm 0.22) \times 10^{-6}$	$-1.336 \pm 0.048$	79	$1.32 \times 10^{-4}$	$1.83 \times 10^{-5}$
100	$(1.62 \pm 0.12) \times 10^{-6}$	$-1.303 \pm 0.019$	92	$2.67 \times 10^{-5}$	$7.83 \times 10^{-6}$
150	$(7.34 \pm 0.15) \times 10^{-7}$	$-1.273 \pm 0.002$	96	$1.01 \times 10^{-5}$	$5.21 \times 10^{-6}$
AZ31–8Li					
0	$(7.08 \pm 0.81) \times 10^{-5}$	$-1.321 \pm 0.013$	–	–	$2.13 \times 10^{-4}$
10	$(3.71 \pm 0.11) \times 10^{-4}$	$-1.293 \pm 0.017$	–	$2.34 \times 10^{-3}$	$1.40 \times 10^{-3}$
50	$(6.52 \pm 1.01) \times 10^{-6}$	$-1.250 \pm 0.068$	90	$1.79 \times 10^{-3}$	$7.68 \times 10^{-5}$
100	$(6.26 \pm 0.28) \times 10^{-6}$	$-1.235 \pm 0.013$	91	$3.69 \times 10^{-5}$	$5.30 \times 10^{-5}$
150	$(1.75 \pm 0.37) \times 10^{-6}$	$-1.220 \pm 0.010$	98	$1.54 \times 10^{-5}$	$1.94 \times 10^{-5}$
AZ31–12Li					
0	$(1.47 \pm 0.9) \times 10^{-4}$	$-1.290 \pm 0.027$	–	–	$6.31 \times 10^{-4}$
10	$(8.44 \pm 1.05) \times 10^{-4}$	$-1.281 \pm 0.030$	–	$6.65 \times 10^{-2}$	$3.41 \times 10^{-3}$
50	$(1.29 \pm 0.89) \times 10^{-4}$	$-1.278 \pm 0.022$	12	$3.73 \times 10^{-4}$	$5.63 \times 10^{-4}$
100	$(1.59 \pm 0.32) \times 10^{-5}$	$-1.263 \pm 0.026$	89	$7.56 \times 10^{-5}$	$3.80 \times 10^{-4}$
150	$(1.63 \pm 0.20) \times 10^{-5}$	$-1.225 \pm 0.039$	89	$3.84 \times 10^{-5}$	$1.95 \times 10^{-4}$

concentration of the inhibitor 50 mM or higher, it was possible to register a rapid change in the slope on the anodic polarization curves recorded for AZ31–8Li, and AZ31–12Li alloys, corresponding to the breakdown potential,  $E_{\text{br}}$ . This provides additional evidence for the formation of a surface protective layer.

The calculated values of  $i_{\text{corr}}$  at low concentrations of the inhibitor (10 mM of  $\text{Na}_2\text{MoO}_4$ ) increased for all examined alloys. This indicates that at low concentrations aqueous molybdate is not able to effectively suppress corrosion at all active surface sites. This results in an increased current density over unprotected areas and, consequently, an increased corrosion rate. The same behavior was previously observed for the WE43 and AZ31 alloys in the case of the molybdate and permanganate inhibitors [34,44,45]. At higher added concentrations,  $\text{Na}_2\text{MoO}_4$  caused a pronounced decrease in  $i_{\text{corr}}$ . The highest IE calculated by Eq. (3) was 89–97% in solutions containing 100 or 150 mM of the inhibitor. To additionally evaluate the inhibition efficacy of partial electrode processes, the values of the current densities  $i_{\text{a}}$  and  $i_{\text{c}}$  were extracted at selected potentials of  $-1.10$  and  $-1.45$  V, respectively, laying on anodic and cathodic branches of polarization curves. The anodic and cathodic current densities decreased two orders of magnitude (150 mM of  $\text{Na}_2\text{MoO}_4$ ), supporting the results of the Tafel fit and reliable corrosion inhibition.

To calculate the polarization resistance,  $R_p$ , small-amplitude CV curves were recorded. The obtained values of  $R_p$  and IE values calculated on Eq. (2) are shown in Fig. 6. As for the polarization data described above, low concentrations of the molybdate inhibitor (10 mM) resulted

in a decrease of  $R_p$ . At higher concentrations of  $\text{Na}_2\text{MoO}_4$ , the values of  $R_p$  were gradually increasing reaching the maximum in 0.05 M chloride solution containing 150 mM of  $\text{Na}_2\text{MoO}_4$ . The obtained values of the inhibition efficiency (Eq. (2)) were similar to those of the potentiodynamic measurements.

### 3.2.3. Classical electrochemical impedance spectroscopy

A comprehensive EIS analysis was performed to further understand the mechanism of protective action of  $\text{Na}_2\text{MoO}_4$  inhibitor. The EIS plots

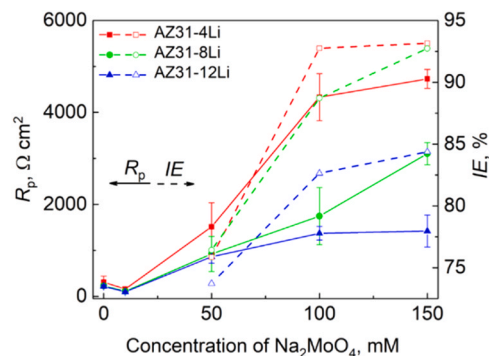


Fig. 6. Polarization resistance of AZ31-xLi alloys in 0.05 M NaCl solutions without and with varying amounts of  $\text{Na}_2\text{MoO}_4$  inhibitor. Solid lines are  $R_p$  and dashed lines are IE values.

of AZ31-xLi alloys obtained in 0.05 M NaCl solution during the classical EIS measurement are shown in Fig. 7. The measurements were performed after the OCP was stabilized for 1000 s (Fig. 4). All obtained Nyquist spectra characteristically display a distorted capacitive loop corresponding to two overlapping time constants at high and medium frequencies and an inductive loop at low frequencies. The recorded EIS spectra are typical for the AZ31 and AZ31-xLi alloys [23,44,45,64,65]. Some spectra also showed an inductive response at high frequencies, which, however, usually originate from used cable connections and were not considered in the spectra analysis. The impedance modulus at low frequencies and the capacitive response at middle frequencies analyzed from Bode plots significantly increased in solutions containing the inhibitor (Fig. 7). Such a response indicates improved corrosion resistance of the surface. However, in solutions with 10 mM of the inhibitor, impedance modulus decreased suggesting lower corrosion resistance.

The interpretation of the EIS data was done taking into account the limitations of EIS measurements, especially in the low-frequency region caused by the non-stationarity of the examined system. The quantitative assessment of the protective effect of the inhibitor based on the EIS data is usually performed using Eq. (2) and charge transfer resistance  $R_{ct}$  or polarization resistance  $R_p$  values. From EIS spectra,  $R_{ct}$  may be determined as the impedance value when  $Z'' \rightarrow 0$ , while  $R_p$  can be estimated as the low-frequency intersection of the impedance with the x-axis when the frequency  $f \rightarrow 0$ . In all examined conditions, the classical EIS measurement clearly showed low-frequency inductive loops in the Nyquist representation, showing a great difference between impedance values based on  $R_{ct}$  and  $R_p$ . Most often, such inductive loops are assigned to the relaxation processes of adsorbed intermediates of the corrosion process [66,67]. However, to provide a repeatable and reliable impedance spectrum, the measured system must fulfill the requirement of stationarity. Classical EIS measurements of Mg alloys' corrosion are often largely affected by the system's non-stationarity [68], which might

cause the occurrence of the low-frequency inductive tail and thus provide uncertainty in the interpretation of the obtained results [68,69]. To mitigate this limitation, we propose to implement dynamic DEIS measurements described in the next part of this submission. At the same time, to correctly address the parameters of the equivalent circuit and fitting error of the classical EIS measurements and compare them with the DEIS results, the inductive part was excluded from the spectra fitting. This was done by selecting the frequency interval in the fitting software where no inductive response was registered. The used equivalent circuit is shown in Fig. 7a. In this approach,  $R_s$  corresponds to the resistance of the solution,  $R_1$  represents the resistance of the surface oxide/hydroxide or protective (inhibitor) film [70–73],  $CPE_1$  is a capacitive response of this film [34,44,70,73],  $R_2$  is the charge transfer resistance, and  $CPE_2$  is a constant phase element for the electrochemical double layer [44,66]. The element CPE in the circuit was used to address the capacitive response of a non-uniform surface of studied AZ31-xLi alloys. The impedance of CPE can be expressed as:

$$Z_{CPE} = \frac{1}{Y_0 (j\omega)^n} \quad (4)$$

where  $Y_0$  is the CPE constant,  $j$  is the imaginary unit,  $\omega$  is the radian frequency, and  $n$  is the mathematical factor.

The results of the spectra fitting are summarized in Table 3. It can be seen that both  $R_1$  and  $R_2$  parameters increased significantly compared to the uninhibited solution as the concentration of the inhibitor in the solution was 50 mM or more.

Calculations of  $IE$  based on the classical EIS data were done based on the values of  $R_{ct}$  and the surface film resistance  $R_1$ , with the latter being further used in the interpretation of the DEIS data. The obtained values are listed in Table 3. The highest  $IE$  values were recorded when 150 mM of the inhibitor was added to the solutions. The values of the protective

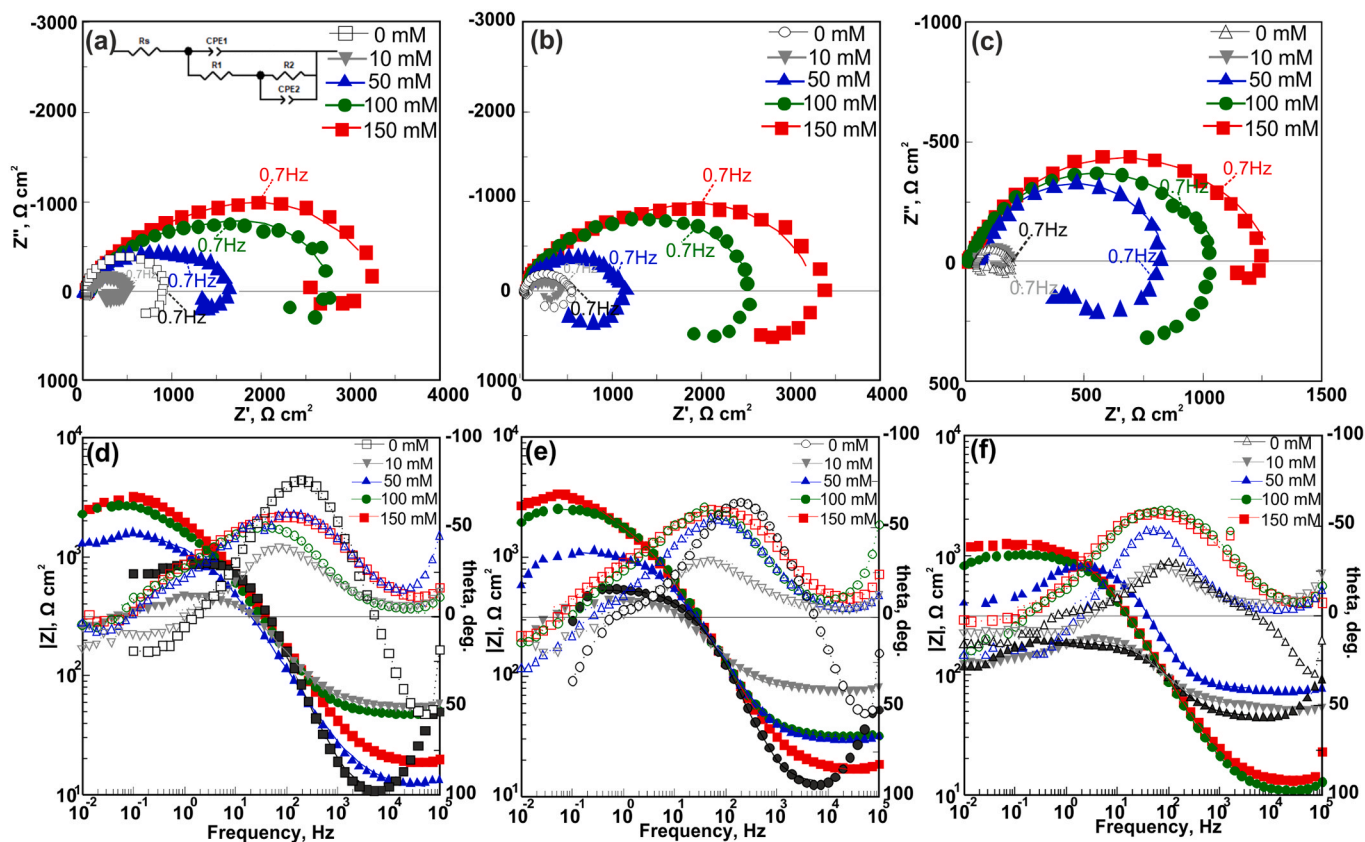


Fig. 7. Nyquist and Bode EIS plots of AZ31–4Li (a, d), AZ31–8Li (b, e), and AZ31–12Li (c, f) in 0.05 M NaCl in the absence and presence of  $\text{Na}_2\text{MoO}_4$ . Symbols represent experimentally obtained data and lines are fitting results with equivalent circuit shown as an inset in (a).

**Table 3**

The results of the fitting experimental EIS data with an equivalent circuit shown in Fig. 7a and a standard deviation value of three independent measurements.

Concentration of inhibitor, mM	$R_1, \Omega \text{ cm}^2$	$R_2, \Omega \text{ cm}^2$	$Y_0, \mu\Omega^{-1} \text{ cm}^{-2} \text{ s}^n$	$n_1$	$Y_0, \mu\Omega^{-1} \text{ cm}^{-2} \text{ s}^n$	$n_2$	$R_{ct}, \Omega \text{ cm}^2$	IE ( $R_{ct}$ ), %	IE ( $R_1$ ), %
AZ31–4Li									
0	727±64	134±39	15±3	0.95±0.03	15±5	0.95±0.03	861	–	–
10	361±44	67±28	48±6	0.77±0.02	24±16	0.99±0.01	428	–	–
50	1450±82	329±73	90±4	0.72±0.01	100±20	0.90±0.01	1779	52	49
100	1520±78	783±67	26±2	0.86±0.01	82±22	0.91±0.15	2303	63	52
150	2410±55	810±71	54±2	0.77±0.01	290±70	0.85±0.10	3220	73	70
AZ31–8Li									
0	305±66	215±47	13±7	0.97±0.02	120±50	0.77±0.15	520	–	–
10	303±10	55±15	50±5	0.81±0.01	140±20	0.89±0.05	358	–	–
50	762±88	327±76	47±6	0.80±0.20	190±60	0.80±0.20	1089	52	59
100	2063±133	505±48	54±2	0.78±0.01	390±90	0.92±0.08	2568	79	85
150	2093±84	1183±380	60±10	0.76±0.01	260±120	0.91±0.03	3276	84	86
AZ31–12Li									
0	142±15	2±	69±1	0.81±0.5	240±100	0.92±0.05	144	–	–
10	135±5	5±7	60±13	0.85±0.5	470±150	0.97±0.01	140	–	–
50	732±27	35±18	22±8	0.89±0.01	77±5	0.95±0.10	767	81	80
100	1061±73	12±45	82±14	0.77±0.05	360±30	0.90±0.09	1073	86	87
150	1266±106	275±68	87±35	0.75±0.01	220±100	0.89±0.03	1541	91	88

action calculated based on both parameters were comparable to each other and increased with an increase in the content of Li in alloys.

### 3.2.4. Dynamic electrochemical impedance spectroscopy

As stated above, the non-stationarity of the measured system can cause a significant effect on the impedance measurement of Mg alloys. Therefore, to minimize the impact of the system's non-stationarity, dynamic DEIS measurements were also performed. In the selected frequency interval (22000–0.7 Hz) the measurement time of each spectrum is less than 1 s and the OCP is measured before each EIS spectrum, which allows to perform the measurement in quasi-stationary conditions [50]. The DEIS spectra of AZ31-xLi alloys obtained in the solutions with and without the molybdate inhibitor during 70 minutes of immersion are shown in Fig. 8, while selected Bode plots, corresponding to the conditions similar to those examined by classical EIS are shown in Fig. 9.

The impedance response of all alloys in the 0.05 M NaCl solution (Fig. 8a–c, Fig. 9a–c) without the inhibitor showed similar features. All obtained spectra showed one capacitive loop with a clear sign of

inductive response even for the DEIS multisine signal. Compared to the classical EIS measurements, this inductive response clearly originates from ionized species generated in the frame of the corrosion of the examined alloys. The alloy with less Li had greater corrosion resistance, according to a comparison of the DEIS spectra acquired throughout the same time periods. For all alloys, the radii of the DEIS spectra decreased with immersion time, showing high corrosion rates and weak resistance of the formed surface films of corrosion products. After 2000 s, the radii and shapes of the spectra are comparable for all alloys (Fig. 8a–c), suggesting that a layer of corrosion products was formed on the surface, which to some extent controls corrosion rate.

To further examine the protective action of sodium molybdate, it was gradually added into the 0.05 M NaCl solution after initial pre-exposure for 10 min in the non-inhibited solution (Fig. 8d–f). The introduction of the molybdate inhibitor significantly increases the radii of the DEIS spectra of all studied alloys. It suggests rapid adsorption of the inhibitor on the surface with the formation of a protective layer, which suppresses the active corrosion of alloys. The comparison of the spectra obtained in

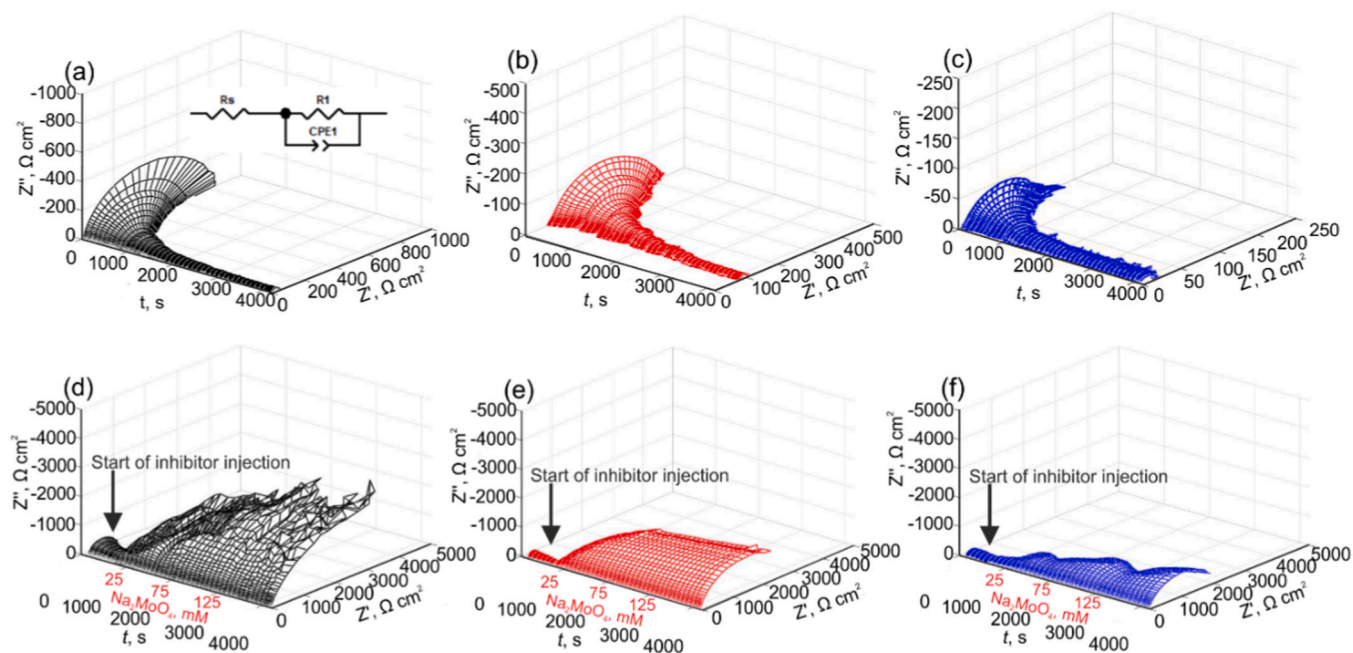


**Fig. 8.** Nyquist DEIS plots of AZ31–4Li (a, d), AZ31–8Li (b, e), and AZ31–12Li (c, f) in 0.05 M NaCl without (a–c) and with (d–f) gradually increased amounts of  $\text{Na}_2\text{MoO}_4$  inhibitor. The equivalent circuit used for data fitting is shown as inset in (a).

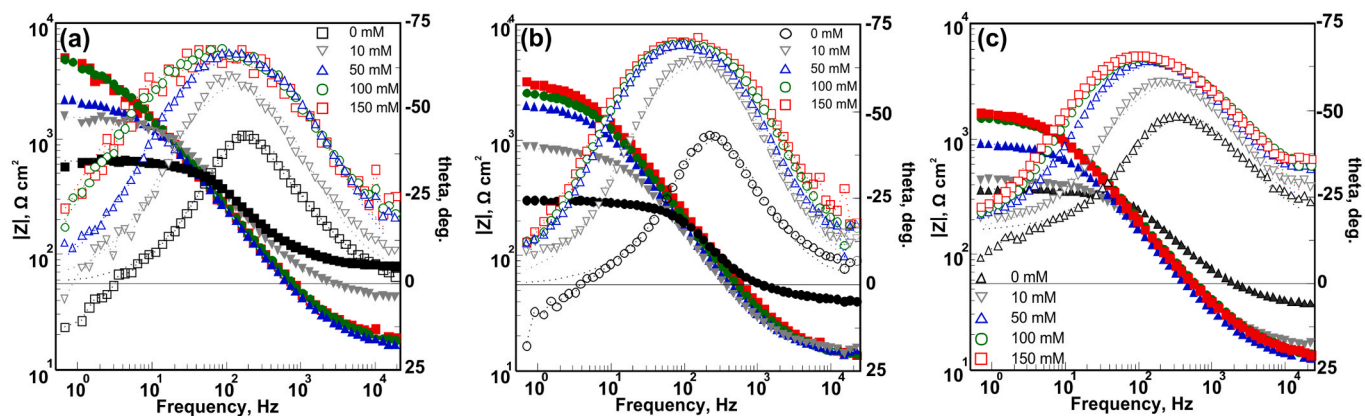


Fig. 9. Bode DEIS plots of AZ31-4Li (a), AZ31-8Li (b), and AZ31-12Li (c) in 0.05 M NaCl without and with gradually increased amounts of  $\text{Na}_2\text{MoO}_4$  inhibitor. Conditions marked as 0 mM show the last DEIS spectrum registered in 0.05 M NaCl before initiation of the inhibitor addition.

the conditions with and without the inhibitor confirmed that the content of Li in AZ31-xLi Mg alloys has a strong impact on the corrosion inhibition values. The highest initial increase in the impedance values was observed for the AZ31-4Li alloy. The further increase in the inhibitor concentration results in a monotonous increase in the impedance values, with its rate decreasing in the row AZ31-4Li  $\rightarrow$  AZ31-8Li  $\rightarrow$  AZ31-12Li alloy. Nevertheless, for all alloys, the molybdate inhibitor showed high effectiveness, while the inhibition mechanism strongly depends on the concentration of the inhibitor in the solution. A similar tendency was previously reported for the AZ31 and WE43 Mg alloys [34,44].

The comparison of the 2D EIS and DEIS measurement spectra in the solutions containing the same amounts of the inhibitor (Fig. S2 in Supplementary Information) shows that the impedance values were usually higher in the case of DEIS measurements. These results clearly show the effect of the system nonstationarity and exposure time on the classical EIS measurement. Therefore, the results of the DEIS measurements should be considered more reliable, while both techniques showed comparably high inhibition effectiveness of the molybdate inhibitor.

For the DEIS measurement, the low-frequency range was limited to 0.7 Hz to ensure system stationarity during the measurement. Inhibition of the corrosion processes provided by dissolved molybdate ions resulted in the absence of the inductive response registered in the inhibited solutions. The lowest frequency applied in the DEIS measurement describes the impedance of the surface film of Mg oxide/hydroxide (in 0.05 M NaCl) and Mo-rich species (in molybdate-containing solutions) [50]. To analyze the DEIS data in all conditions, the equivalent circuit shown in Fig. 8a was used. Note, that in the uninhibited conditions, the inductive part was not considered to provide an easier comparison of the

data. In the equivalent circuit, again  $R_s$  was assigned as the solution resistance,  $R_1$  represents the resistance of the surface oxide/hydroxide or protective film [70–73], and  $\text{CPE}_1$  is a capacitive response of this film [34,44,70,73]. The dynamics of the change of the circuit parameters in time is shown in Fig. 10.

The values of  $R_1$  in 0.05 M NaCl without the inhibitor were rapidly decreasing in the first 1000 s of the experiment (inset to Fig. 10a). Afterwards, the decrease was not so prominent, suggesting the occurrence of steady active corrosion of the surface partially covered with a layer of corrosion products. After ca. 3000 s the values of  $R_1$  in 0.05 M NaCl become stable in time. In the experiments with the gradual addition of sodium molybdate into 0.05 M NaCl solution, the value of  $R_1$  corresponds to the resistance of the Mo-rich surface film formed on the surface and it started to increase rapidly when the first portions of the inhibitor were added into the solution. It confirms the rapid adsorption of the inhibitor on the surface of the AZ31-xLi alloys and a rapid protective activity on their surface. In the case of the CPE constant  $Y_0$  (Fig. 10b), its values were almost one order of magnitude lower in the inhibited solutions, also supporting the high efficiency of the inhibitor.

To calculate the effective capacitance of the surface,  $C_{\text{eff}}$ , based on the DEIS data, the following equation was used [74]:

$$C_{\text{eff}} = Y_0^{1/n} \left( \frac{R_s R_1}{R_s R_1} \right)^{(1-n)/n} \quad (5)$$

The calculated values are shown in Fig. 10c. For all examined conditions the value of  $C_{\text{eff}}$  was in the range of  $10^{-4}$ – $10^{-3}$  F/cm<sup>2</sup>, which is typical for oxide protective layers on metal surfaces [74].

Since the rate of the inhibitor supply into the solution is known and

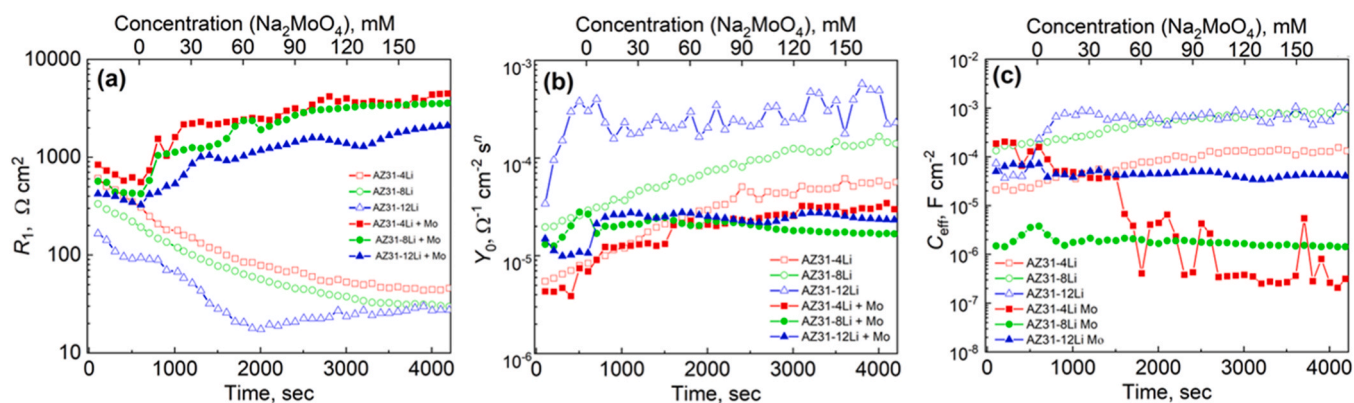


Fig. 10. Evolution of parameters of equivalent circuit used for the analysis of DEIS data. Open markers correspond to 0.05 M NaCl (spectra in Fig. 8a–c) and filled markers describe 0.05 M NaCl with molybdate inhibitor (spectra in Fig. 8d–f). The top x-axes correspond to the concentration profile of  $\text{Na}_2\text{MoO}_4$  in solutions and are valid for only filled markers.

constant, the extracted parameters of the multisine impedance monitoring in the solutions with and without the inhibitor can be assigned to the instant concentration of the molybdate inhibitor in the examined solutions at a given time point. Therefore, inhibition effectiveness,  $IE$ , can also be estimated from the DEIS data using Eq. (2) [50]. The calculated values are listed in Fig. 11. Opposite to polarization (Table 2) and classical EIS (Table 3) results, the positive values of  $IE$  were registered for all concentrations of the inhibitor. The values of  $IE$  were rapidly increasing at low concentrations of the inhibitor for all alloys and then remained almost constant after reaching the concentration of the inhibitor of ca. 35 mM. The stable inhibition effect of ca. 94, 93, and 88% for AZ31–4Li, AZ31–8Li, and AZ31–12Li, respectively, was calculated from the measurements. The obtained results suggest rapid interaction of the inhibitor with the surface of AZ31-xLi Mg alloys.

### 3.3. Post-corrosion surface analysis

In this section, corrosion experiments of AZ31-xLi alloys in 0.05 M NaCl solution without and with 150 mM of the molybdate inhibitor were performed to understand the mechanism of the inhibition action because this concentration provides high inhibition effectiveness. The surface morphology as well as the surface film composition after corrosion were analyzed.

#### 3.3.1. Surface morphology and EDX elemental analysis

The surface morphologies of AZ31-xLi alloys after corrosion in the 0.05 M sodium chloride solution for 5 min, 1, and 24 h is shown in Fig. 12. Selective corrosion of the  $\beta$ -Li phase was clearly visible already after 5 min of immersion in the chloride media (Fig. 12a) for AZ31–8Li, and AZ31–12Li. After 1 h of corrosion, all samples undergo general corrosion of the alloys' matrix phases. At the same time, local corrosion attack around Al- and Mn-rich IMPs was noted. The regions around spots of severe local corrosion were seen to be covered with a layer of corrosion products. The surface of the alloys' matrix was also covered by a layer of corrosion products and corrosion damage increased with an increase in Li content in the alloy. In the case of the AZ31–8Li alloy, the presence of filiform corrosion was observed, which most probably occurred on the boundaries of  $\alpha$  and  $\beta$  phases [23,65]. However, prolonged exposure for 24 h to the corrosive environment resulted in a much more pronounced corrosion attack. An uneven, thick layer of corrosion products covered the surface. The structure of this layer differs somewhat depending on the Li content in the alloy. The difference in the corrosion morphologies between studied alloys is explained by the different phase composition of the alloys (Fig. 2) and pH values in the near-surface layer of the electrolyte and, accordingly, different thicknesses and compositions of the formed layer of corrosion products.

The results of the EDX analysis (Table 4) confirmed that the formed surface films primarily contain magnesium, most probably in the form of

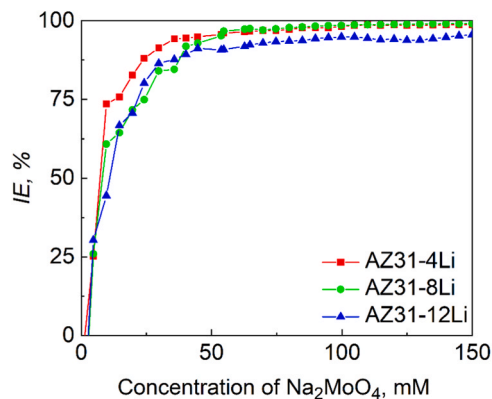


Fig. 11. Evolution of inhibition efficiency  $IE$  depending on the concentration of molybdate inhibitor in 0.05 M NaCl solution.

oxide/hydroxide layers. Aluminum was also observed in rather high amounts (up to 2.6 at%) at the majority of examined spots. After 24 h of exposure to the corrosive environment, the oxygen content in the composition of surface films increased, which may be due to the formation of a thick layer of oxide-hydroxide passive films.

Fig. 13 shows SEM images of the AZ31-xLi alloys immersed in the 0.05 M NaCl solution with 150 mM of sodium molybdate for 1 and 24 h. The surface morphology of all examined alloys was quite different compared to the solution without the inhibitor (Fig. 12). No regions of severe local corrosion attack were seen on the surface, except for some local pitting on the surface of the AZ31–12Li alloy. The formation of a protective Mo-containing layer is clearly seen on the surface of all alloys. After 24 h of exposure, the surfaces of AZ31–4Li and AZ31–8Li alloys do not show areas of severe corrosion attack, while some areas are covered with thick precipitate layers rich in Mo (Table 5), forming passive layers, most probably over IMPs. However, the surfaces of AZ31–12Li contained some areas of local corrosion attack around IMPs, which is due to the higher local reactivity of this alloy. Nevertheless, no prominent corrosion attack was observed supporting the high inhibition activity of molybdate. The point EDX analysis (Table 5) confirmed the presence of molybdate in the surface layers and the formation of a Mo-rich protective layer over the surface of all examined alloys. The surface layers also contain hydrated oxide/hydroxide Mg species, forming corrosion products with varying stoichiometry. Therefore, the relative Mo/O ratio cannot be reliably assigned [34,75]. However, it confirmed that the molybdate inhibitor forms surface protective layers on the surface of AZ31-xLi alloys.

#### 3.3.2. Raman spectroscopy

To further understand the mechanism of corrosion and its inhibition for the AZ31-xLi alloys, Raman spectra were acquired. Optical images of the surfaces selected for Raman measurements are shown in Fig. 14 and obtained characteristic Raman spectra are shown in Fig. 15.

Examination of corrosion mechanisms of Mg alloys by Raman measurements was previously reported in [47,76,77]. In the present contribution and our previous experiments [44], the analysis of Mg-rich surface layers was based on the low-wave number region (200–1200  $\text{cm}^{-1}$ ), where both  $\text{Mg}(\text{OH})_2$  and Mo-rich species can be analyzed [34,44]. Raman spectra of all alloys after exposure to 0.05 M NaCl solution without inhibitor for 1 h were similar and showed two characteristic Raman bands at 280 and 443  $\text{cm}^{-1}$ , corresponding to  $\text{Mg}(\text{OH})_2$  [76,78]. After 24 h of the exposure to uninhibited solutions resulted in the appearance of the Raman band at 1094  $\text{cm}^{-1}$ , which was assigned to the formation of magnesium or lithium carbonates on the surface, probably by the reaction with  $\text{CO}_2$  dissolved in the electrolyte [79,80]. Moreover, we cannot exclude the formation of surface carbonate layers already after 1 h of exposure. However, the thickness of these layers might be not enough for Raman analysis [48].

Raman spectra of the surfaces obtained after corrosion experiments in molybdate-containing solutions showed additional Raman bands associated with Mo-rich compounds. Molybdenum compounds in aqueous media can present in different oxidation states and coordination geometries [81]. Therefore, interpretation of the results of Raman analysis should consider valence states and possible oligomerization degree [34,42,44]. The main Raman band located at 880–1000  $\text{cm}^{-1}$  is typically associated with Mo(VI) species and corresponds to  $\nu_{\text{sym}}(\text{Mo}-\text{O})$  vibrations. Its position is very sensitive to the coordination geometry, the chain length, and the hydration degree of molybdate species [82]. Raman spectra of all alloys after 1 h of corrosion experiments showed bands at 1004, 996, and 265  $\text{cm}^{-1}$ , which are typical for hydrated molybdenum(VI) oxide,  $\text{MoO}_3(\text{H}_2\text{O})_3$  [83–85]. The Raman band at 1110  $\text{cm}^{-1}$  can be assigned to polyoxomolybdate species or  $\text{MoO}_x$  oxides, which are formed on the surface due to a partial reduction of adsorbed molybdate ions [42]. Raman bands at 942  $\text{cm}^{-1}$  correspond to  $\text{Mo}_7\text{O}_6^{24-}$  [86]. Raman bands at 321 and 911  $\text{cm}^{-1}$  were assigned to

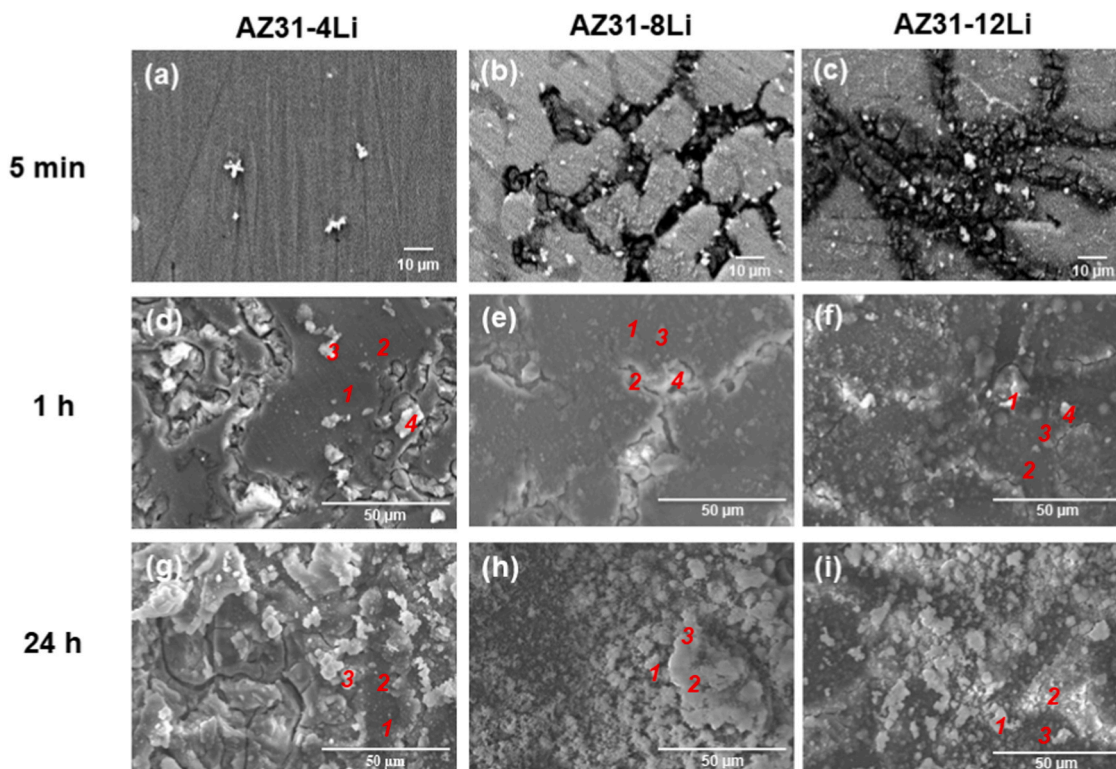


**Fig. 12.** SEM images of the AZ31-4Li (a, d, g), AZ31-8Li (b, e, h), and AZ31-12Li (c, f, i) surface after 5 min (a–c) 1 h (d–f), and 24 h (g–i) exposure to 0.05 M NaCl solution. Numbers correspond to regions analyzed by EDX analysis (Table 4).

**Table 4**

Elemental composition of the surface of AZ31-xLi alloys after 1 and 24 h of exposure to 0.05 M NaCl without inhibitor. Point labels correspond to those marked in Fig. 12.

Alloy	Point	Elemental composition, at%			
		Mg	Al	O	Cl
After 1 h					
AZ31-4Li	1	82.8	1.1	6.8	9.4
	2	61.6	1.3	20.3	16.8
	3	7.8	–	6.9	85.4
	4	82.3	0.4	16.0	1.3
AZ31-8Li	1	97.4	2.6	–	–
	2	76.5	–	16.4	7.2
	3	24.5	2.1	53.6	19.8
AZ31-12Li	4	34.0	2.0	55.2	7.1
	1	37.5	–	55.5	7.0
	2	65.1	0.4	31.2	3.3
AZ31-12Li	3	82.6	0.6	14.5	2.3
	4	30.1	0.8	52.2	17.0
	After 24 h				
AZ31-4Li	1	65.9	1.6	32.5	–
	2	38.8	1.0	50.4	9.8
	3	37.7	1.0	59.7	1.6
AZ31-8Li	1	37.8	0.5	59.7	2.0
	2	40.7	–	59.3	–
AZ31-12Li	3	41.9	–	58.1	–
	1	38.6	–	61.4	–
AZ31-12Li	2	41.4	1.6	54.6	2.4
	3	63.4	0.4	36.2	–

dimolybdates  $\text{Mo}_2\text{O}_7^{2-}$  [87]. Three characteristic bands at 740, 585, and 569  $\text{cm}^{-1}$  were assigned to molybdenum compounds in lower valence states, such as Mo(IV) oxide  $\text{MoO}_2$  or Mo(VI)–Mo(V), Mo(VI)–Mo(IV), and Mo(V)–Mo(IV) mixed-valence species [42,82,84,88].

After 24 h of exposure to 0.05 M NaCl solutions with 150 mM of the molybdate inhibitor, the signal of  $\text{Mg}(\text{OH})_2$  (Raman band at 443  $\text{cm}^{-1}$ )

dominated in the Raman spectra of all alloys due to the surface coverage by corrosion products. However, weak Raman signals at 896 and 845  $\text{cm}^{-1}$  can be assigned to the symmetric and asymmetric stretching of the terminal Mo=O bonds in crystalline molybdates  $\text{MoO}_4^{2-}$  [34,86, 89]. Importantly, no evidence of the presence of Mo(IV) compounds was observed after 24 h of corrosion experiments.

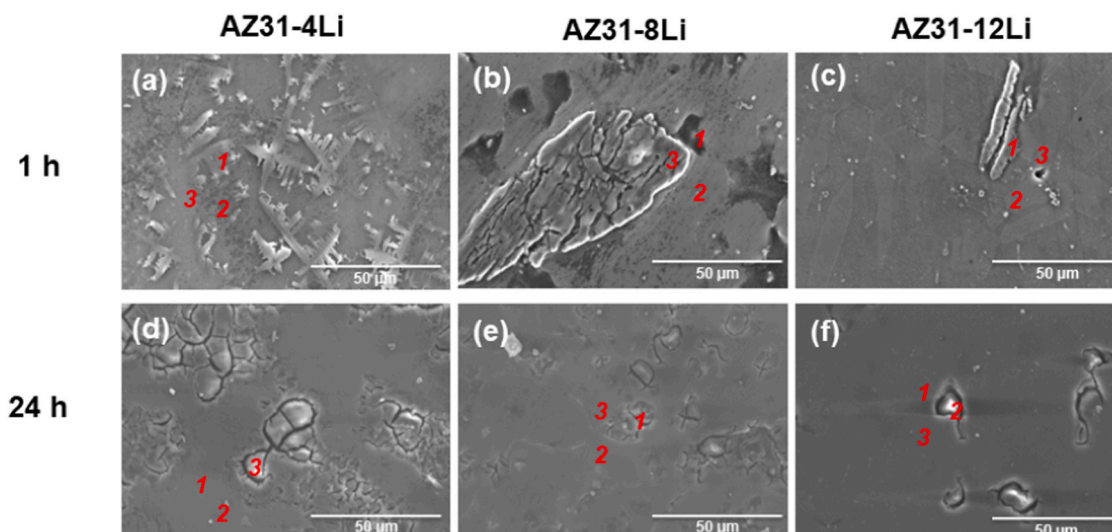
### 3.3.3. XPS spectroscopy

Fig. 16 depicts the results of the high-resolution XPS analysis of the surface of AZ31-xLi alloys after 1 h of exposure to NaCl solution containing 150 mM of the molybdate inhibitor. The phase composition and amount of Li in the alloys have a significant effect on the shape of the obtained spectra. First, XPS spectra shown in Fig. 16a reveal a progressive negative shift of the Mg 1s peak location from 1303.6 eV (for AZ31-4Li) down to 1303.2 eV (for AZ31-12Li), a feature revealing that the alloy surface is covered with the growing amount of Mg hydroxide that probably displaces or covers dense inner MgO layer [51,90,91]. At the same time, the Mg moieties share at the surface increases rapidly, tripling its value.

The interaction of the inhibitor with the surface inevitably leads to the appearance of Mo-rich species in different oxidation states. The formation of Mo(VI) oxides at the surface of all alloys is testified with Mo  $4d_{5/2}$  peak at 232.0 eV [34,42,92]. Its share is the highest in the case of the AZ31-4Li and AZ31-8Li alloys, reaching approx. 12 at% and drops down to 5.3 at% for the AZ31-12Li alloy (Table 6). Additionally, other molybdenum species, Mo(V) and Mo(IV) have been detected in the composition of the surface layers, which share seems to be less affected by the lithium content.

The high-resolution O 1s spectra presented in Fig. 16c support the above observations. The component at 529.9 eV represents Me-O (Me: Mg and Mo) [44,50,91], which dominates at the surface at low Li content and is displaced by hydroxides for AZ31-12Li with Me-OH:Me-O ratio changing from 0.55:1–1.22:1 (Table 6).

The overall observation from the XPS data backs up the



**Fig. 13.** SEM images of AZ31-4Li (a, d), AZ31-8Li (b, e), and AZ31-12Li (c, f) surface after 1 h (a–c) and 24 h (d–f) exposure to 0.05 M NaCl solution with 150 mM of  $\text{Na}_2\text{MoO}_4$ . Numbers indicate regions analyzed by EDX analysis (Table 5).

**Table 5**

Elemental composition of the surface of AZ31-xLi alloys after 1 and 24 h of exposure to 0.05 M NaCl with 150 mM of  $\text{Na}_2\text{MoO}_4$ . Point labels correspond to those marked in Fig. 13.

Alloy	Point	Elemental composition, at%					
		Mg	Al	O	Cl	Mo	Na
After 1 h							
AZ31-4Li	1	31.5	1.3	3.2	36.6		27.4
	2	79.9	0.8	13.8	2.7	1.8	0.9
	3	63.8	1.0	4.0	18.3	1.1	11.8
AZ31-8Li	1	72.6	0.8	17.6	8.2	0.8	–
	2	94.2	2.5	3.3	–	–	–
	3	69.2	2.4	11.1	16.2	1.1	–
AZ31-12Li	1	51.7	8.5	39.8	–	–	–
	2	95.7	1.2	3.2	–	1.0	13.6
	3	67.0	5.2	13.2	–	–	–
After 24 h							
AZ31-4Li	1	91.2	4.2	4.2	–	0.4	–
	2	99.8	0.1	0	–	–	–
	3	88.9	0.5	7.6	–	3	–
AZ31-8Li	1	80.3	1.7	5.5	10.5	0.5	1.5
	2	24.7	6.7	52	9.5	3.3	3.8
	3	93.6	2.3	4.2	–	–	–
AZ31-12Li	1	88.1	0.6	5.1	6.2	–	–
	2	34.1	3.9	57.7	–	4.3	–
	3	88.6	0.9	–	6.2	4.3	–

electrochemical studies, confirming the higher corrosion susceptibility of the alloys with larger lithium additive, where the passive film is replaced by non-stoichiometric corrosion products (primarily magnesium hydroxides).

### 3.4. Mechanism of corrosion and its inhibition

In this section, we summarize the results of the electrochemical measurements and surface analysis and propose the corrosion mechanism of AZ31-xLi alloys in 0.05 M sodium chloride solutions. Implementation of the DEIS approach also allows to provide of a detailed inhibition mechanism by aqueous molybdate species.

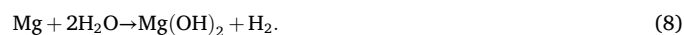
The phase composition of the surface of AZ31-xLi alloys consisted of the alloy matrix and several types of IMPs. The most important difference with the increase of lithium content in AZ31-xLi ( $x = 4, 8, 12$ ) alloys, is the change of the crystal structure from  $\alpha$ -phase hcp (AZ31-4Li) to  $\beta$ -phase bcc (AZ31-12Li) through a mixed  $\alpha + \beta$  phase

(AZ31-8Li). Therefore, the corrosion resistance of examined alloys should be mainly defined by the corrosion resistance of the bulk  $\alpha$ - and  $\beta$ -phases and microgalvanic activity between the alloys' matrix and IMPs. Li et al. [23] reported a decrease in the corrosion rate of Mg-Li alloys in 0.1 M NaCl in the following order  $\text{Mg-7.5Li} > \text{Mg-4Li} > \text{Mg-14Li}$ . However, in the present contribution, a linear decrease in the corrosion resistance with increased Li content was observed in an order  $\text{AZ31-4Li} > \text{AZ31-8Li} > \text{AZ31-12Li}$ . This difference might be attributed to the additional presence of Al and Zn in the composition of the alloys leading to the differences in the composition of IMPs, variations in the heat treatment, and other structural parameters (grain size, IMPs size, etc.).

In the case of AZ31-xLi alloys examined in the present contribution, the surface morphology after corrosion in 0.05 M NaCl solutions includes areas covered by a relatively thin and thick porous layer of  $\text{Mg}(\text{OH})_2$ . Corrosion of the alloys is mainly localized on their matrix and matrix/IMP interfaces, following the mechanism:



The overall reaction is:



As the examined alloys contain high amounts of Li, its selective dissolution from the matrix and IMPs will occur following the reaction:



This process is also accompanied by hydrogen evolution on Eq. (7), which can promote the deposition of a surface Li hydroxide layer:



with the overall reaction:



The analysis of the track of the OCP of examined alloys and pH of solutions (Fig. 4) shows that these processes, especially the selective dissolution of lithium, are very rapid. The intensification of the process of selective dissolution of Li will also be facilitated by the formation of microgalvanic pairs between phases of the alloys with different electronegativity. However, the surface of all alloys is covered by a layer of corrosion products within a few minutes, as evidenced by the

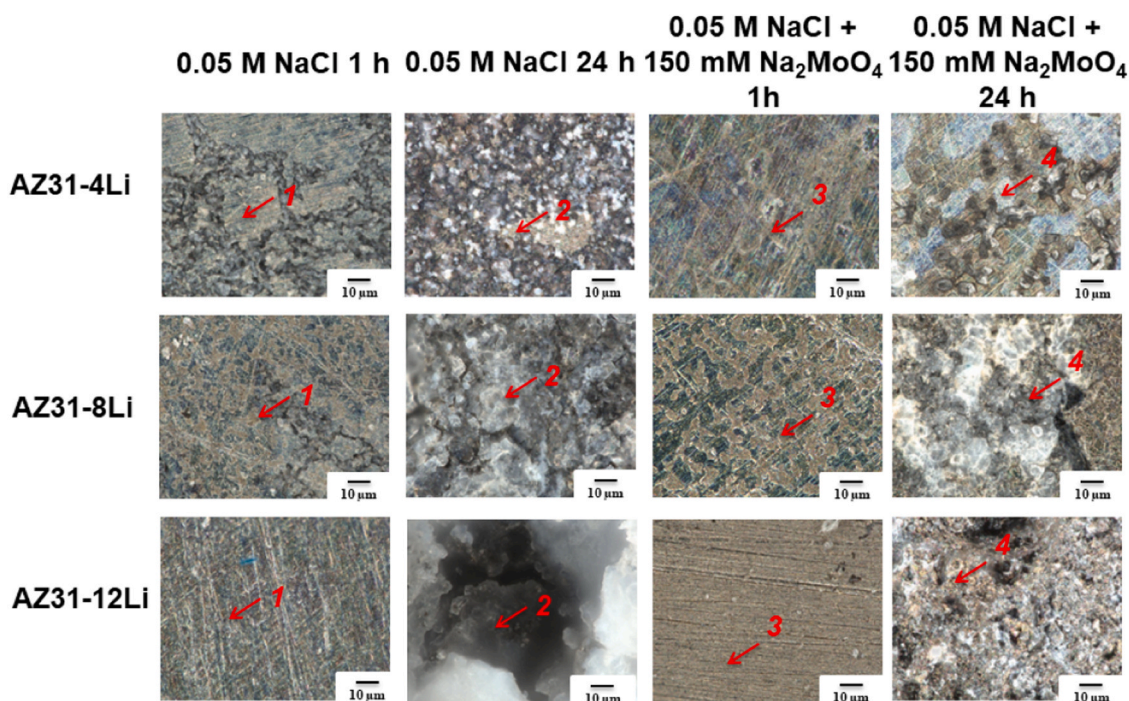


Fig. 14. Optical images of AZ31-4Li (top row), AZ31-8Li (middle row), and AZ31-12Li (bottom row) surface after 1 and 24 h exposure to 0.05 M NaCl solution without and with 150 mM of  $\text{Na}_2\text{MoO}_4$ . Numbers indicate regions analyzed by Raman spectroscopy (Fig. 15).

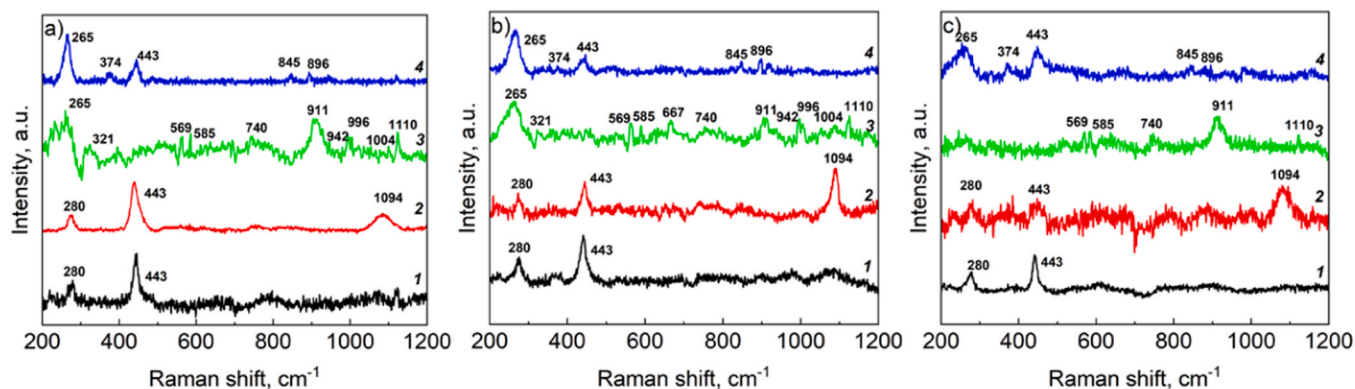


Fig. 15. Raman spectra of AZ31-4Li (a), AZ31-8Li (b), and AZ31-12Li (c) after 1 (1, 3) and 24 h (2, 4) exposure to 0.05 M NaCl solution without (1, 2) and with (3, 4) 150 mM of  $\text{Na}_2\text{MoO}_4$ . Numbers indicate regions analyzed by Raman spectroscopy (Fig. 14).

stabilization of the OCP and further confirmed by the results of DEIS measurements (Fig. 8a–c). The stabilization time decreased as the content of Li in the alloy increased, which might be attributed to the formation of surface films with higher protective ability. The solubility of lithium hydroxide is rather high and in naturally aerated solutions, corrosion products can further react with dissolved carbon dioxide forming stable carbonate surface films on reactions:



The presence of surface carbonates was confirmed by Raman (Fig. 15) and C 1 s XPS spectra (not shown). Nevertheless, the protective ability of the formed surface layers is not enough, and corrosion attack increased after 24 h of exposure to 0.05 M NaCl solution under the influence of aggressive chloride ions and possible microdefects in the formed complex morphologies (Fig. 12).

Our electrochemical data demonstrated that the use of the

molybdate inhibitor significantly affects the corrosion behavior of all examined AZ31-xLi alloys. In aqueous media, molybdate ions retard corrosion of the examined alloys by forming a protective insoluble film over the active surface areas. Nevertheless, as for other Mg alloys [34, 44], it is essential to supply high concentrations of the inhibitor in the electrolyte, especially in the initial stages of the inhibition, to ensure effectiveness (Figs. 5–7). Interestingly, the results of instant DEIS measurements report inhibition effectiveness even for small portions of the inhibition (Fig. 10). However, utilization of low concentrations of molybdates seems to be inefficient at long exposure times. Therefore, in the mechanism below we assume relatively high concentrations of the inhibitor in the solution (above 100 mM) to provide reliable inhibition.

The aqueous chemistry of molybdates is rather complex and many ionic forms are present in aqueous solutions depending on their pH [42, 86]. Due to the processes of the alloys' corrosion described by Eqs. (6)–(11), the pH in the near electrode area is alkaline. Therefore, mostly monomolybdates will be present in the solution [34]. As supported by the DEIS data (Fig. 10), a rapid adsorption of molybdate ions on the

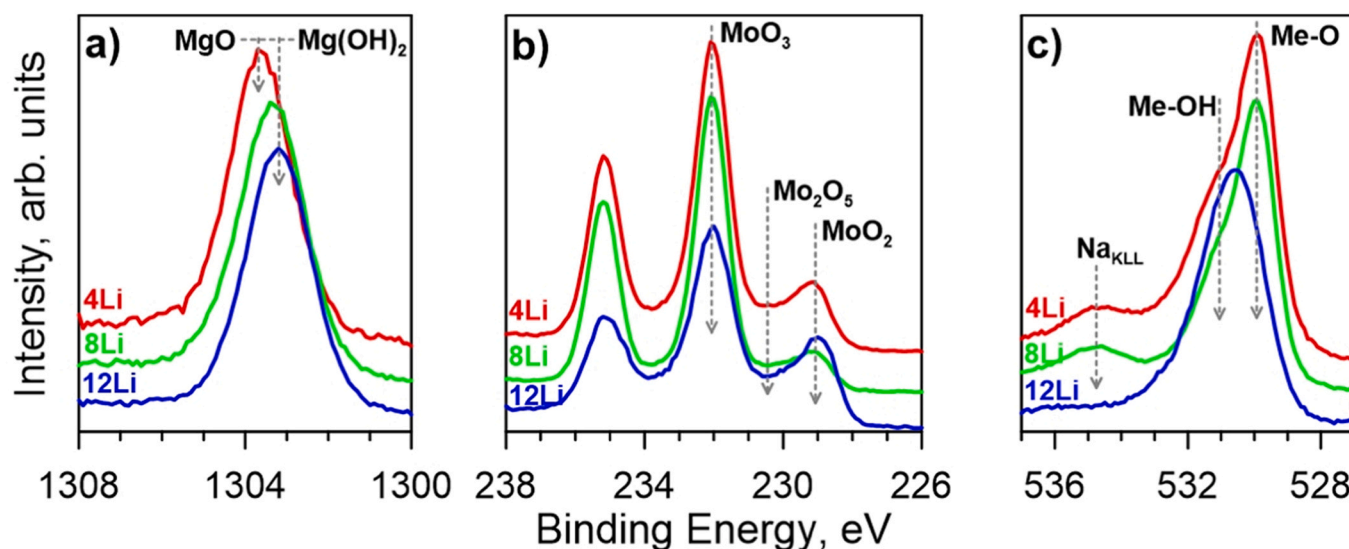


**Fig. 16.** High-resolution XPS spectra recorded in a) Mg 1 s; b) Mo 3d, and c) O 1 s core level binding energy range for AZ31–4Li, AZ31–8Li, and AZ31–12Li alloys after 1 h corrosion exposure in 0.05 M NaCl with 150 mM  $\text{Na}_2\text{MoO}_4$  inhibitor.

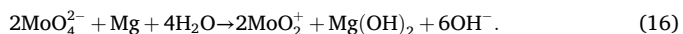
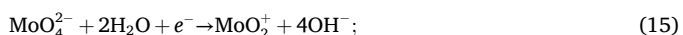
**Table 6**

Surface chemical composition of AZ31-4Li, AZ31-8Li, and AZ31-12Li after 1 h corrosion exposure in 0.05 M NaCl with 150 mM  $\text{Na}_2\text{MoO}_4$  inhibitor based on XPS analysis.

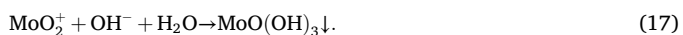
Compound	Mg 1 s		Mo 4d			O 1 s	
	MgO/Mg(OH) <sub>2</sub>		MoO <sub>3</sub>	Mo <sub>2</sub> O <sub>5</sub>	MoO <sub>2</sub>	Me-OH	Me-O
BE	1303.6–1303.2		232.0	230.4	229.1	531.2	529.9
AZ31–4Li	8.3		11.7	2.1	3.3	26.7	47.9
AZ31–8Li	13.3		12.2	1.4	2.0	23.7	47.4
AZ31–12Li	25.2		5.3	1.4	3.2	35.6	29.3

surface is the first stage in the inhibition mechanism of AZ31-xLi alloys. The adsorption preferably occurs on the active areas of the surface. However, it is mostly uniform with time and after 24 h of corrosion, almost the whole surface of all alloys was covered with a Mo-rich layer (Fig. 13).

The high reactivity of Mg and Li promotes the reduction of adsorbed molybdates with the formation of Mo(IV) oxide and mixed Mo(V)-Mo(VI) polymolybdate species, as confirmed by Raman (Fig. 15) and XPS data (Fig. 16, Table 6):



As the last step, formed  $\text{MoO}_2^+$  ions can interact with hydroxide ions  $\text{OH}^-$  in the near interface area:



The insoluble hydroxide formed in the process Eq.(17) provides a high corrosion protection effect. It should be noted that after 24 h of corrosion experiments, the amount of molybdate on the surface decreased compared to that after 1 h of testing. It might indicate that the high corrosion activity of AZ31-xLi alloys contributes to further local corrosion attack.

#### 4. Conclusions

In this work, the effect of sodium molybdate on the corrosion

mechanism of lithium-containing AZ31-xLi ( $x = 4, 8, \text{ and } 12 \text{ wt}\%$ ) magnesium alloy was examined. The corrosion protection effectiveness of molybdate was evaluated depending on its concentration in 0.05 M NaCl solution and associated with the composition of the surface Mo-rich films. The following conclusions can be drawn:

1. The microstructure of the AZ31-xLi ( $x = 4, 8, \text{ and } 12 \text{ wt}\%$ ) magnesium alloys strongly depends on the concentration of Li in the alloy. The alloys consist of  $\alpha$ -Mg (AZ31–4Li),  $\alpha$ -Mg and  $\beta$ -Li (AZ31–8Li), and  $\beta$ -Li (AZ31–12Li) matrix phases with micrometer-sized Mg-Al, Al-Mn, and Al-Zn IMPs distributed in matrix phases.
2. Potentiodynamic polarization and classical EIS data revealed that aqueous molybdate at high concentrations ( $>50 \text{ mM}$ ) leads to a significant decrease (up to ca. 95% for 150 mM of  $\text{Na}_2\text{MoO}_4$ ) in the corrosion rate of the AZ31-xLi alloys in 0.05 M NaCl solutions. Application of multisine DEIS measurements allowed for instantaneous monitoring of the inhibition efficiency in time with the values of the inhibition efficiency of ca. 85% at concentrations of molybdate higher than 35 mM.
3. Corrosion of AZ31-xLi ( $x = 4, 8, \text{ and } 12 \text{ wt}\%$ ) magnesium alloys in 0.05 M NaCl solutions results in the formation of thick non-uniform layers of corrosion products. The results of the Raman and XPS spectroscopy confirmed that these layers consist of  $\text{MgO}/\text{Mg}(\text{OH})_2/\text{MgCO}_3/\text{Li}_2\text{CO}_3$ . In the case of 0.05 M NaCl additionally containing aqueous molybdate, stable protective films containing Mo(IV), Mo(V), and Mo(VI) compounds were formed.
4. The corrosion rate of AZ31-xLi ( $x = 4, 8, \text{ and } 12 \text{ wt}\%$ ) Mg alloys increases with the increase in Li content. The corrosion mechanism of the AZ31-xLi surface in 0.05 M NaCl solution mainly localizes on the selective dissolution of the alloys' matrixes around cathodic IMPs and of Li from IMPs. Corrosion inhibition by  $\text{Na}_2\text{MoO}_4$  is achieved by the competitive adsorption of molybdate anions on the active sites of the surface of AZ31-xLi alloys and the formation of a Mo(VI)/Mo(V)/Mo(IV)-rich mixed-valence dense protective layers.

#### CRediT authorship contribution statement

**Maria A Osipenko:** Conceptualization, Data curation, Formal analysis, Investigation, Visualization, Writing – original draft, Writing – review & editing. **Andrei Paspelau:** Investigation. **Aliksandr Kasach:** Formal analysis. **Jacek Ryl:** Formal analysis, Funding acquisition, Investigation. **Konrad Skowron:** Investigation. **Janusz Adamiec:**

Investigation, Resources. **Irina Kurilo**: Conceptualization, Methodology, Supervision, Writing – original draft, Writing – review & editing. **Dzmitry S Kharytonau**: Conceptualization, Formal analysis, Funding acquisition, Investigation, Methodology, Project administration, Resources, Supervision, Validation, Visualization, Writing – original draft, Writing – review & editing.

### Declaration of Competing Interest

The authors declare that they have no known competing financial interests or personal relationships that could have appeared to influence the work reported in this paper.

### Acknowledgments

Dzmitry Kharytonau gratefully acknowledges financial support from the National Science Center (Poland) under research Grant Miniatura no. 2019/03/X/ST4/00749.

Jacek Ryl gratefully acknowledges support by Gdańsk University of Technology under the Aurum Supporting International Research Team Building – ‘Excellence Initiative – Research University’ (2/2021/IDUB/II.1.3).

Maria A. Osipenko gratefully acknowledges support from the Belarusian Republican Foundation for Fundamental Research under grant no. X24MB-008 “Environmentally friendly corrosion inhibitors based on soluble molybdenum(VI) compounds for lithium-containing Mg alloys”.

### Appendix A. Supporting information

Supplementary data associated with this article can be found in the online version at [doi:10.1016/j.corsci.2024.112513](https://doi.org/10.1016/j.corsci.2024.112513).

### Data Availability

Data will be made available on request.

### References

- M.K. Kulecki, Magnesium and its alloys applications in automotive industry, *Int. J. Adv. Manuf. Technol.* 39 (2008) 851–865, <https://doi.org/10.1007/s00170-007-1279-2>.
- M. Esmaily, J.E. Svensson, S. Fajardo, N. Birbilis, G.S. Frankel, S. Virtanen, R. Arrabal, S. Thomas, L.G. Johansson, Fundamentals and advances in magnesium alloy corrosion, *Prog. Mater. Sci.* 89 (2017) 92–193, <https://doi.org/10.1016/j.pmatsci.2017.04.011>.
- P.C. Banerjee, S. Al-Saadi, L. Choudhary, S.E. Harandi, R. Singh, Magnesium implants: prospects and challenges, *Mater. (Basel)* 12 (2019) 1–21, <https://doi.org/10.3390/ma12010136>.
- E. Wierzbicka, B. Vaghefinazari, M. Mojedano, P. Visser, R. Posner, C. Blawert, M. Zheludkevich, S. Lamaka, E. Matytkina, R. Arrabal, Chromate-free corrosion protection strategies for magnesium alloys—a review: part II—PEO and anodizing, *Mater. (Basel)* 15 (2022) 8515, <https://doi.org/10.3390/ma15238515>.
- G. Barati Darband, M. Aliofkhaezrai, P. Hamghalam, N. Valizade, Plasma electrolytic oxidation of magnesium and its alloys: mechanism, properties and applications, *J. Magnes. Alloy.* 5 (2017) 74–132, <https://doi.org/10.1016/j.jma.2017.02.004>.
- K. Gusieva, C.H.J. Davies, J.R. Scully, N. Birbilis, Corrosion of magnesium alloys: the role of alloying, *Int. Mater. Rev.* 60 (2015) 169–194, <https://doi.org/10.1179/1743280414Y.0000000046>.
- M. Deng, L. Wang, D. Höche, S.V. Lamaka, C. Wang, D. Snihirova, Y. Jin, Y. Zhang, M.L. Zheludkevich, Approaching “stainless magnesium” by Ca micro-alloying, *Mater. Horiz.* 8 (2021) 589–596, <https://doi.org/10.1039/D0MH01380C>.
- M. He, L. Chen, M. Yin, S. Xu, Z. Liang, Review on magnesium and magnesium-based alloys as biomaterials for bone immobilization, *J. Mater. Res. Technol.* 23 (2023) 4396–4419, <https://doi.org/10.1016/j.jmrt.2023.02.037>.
- B. Vaghefinazari, E. Wierzbicka, P. Visser, R. Posner, R. Arrabal, E. Matytkina, M. Mojedano, C. Blawert, M. Zheludkevich, S. Lamaka, Chromate-free corrosion protection strategies for magnesium alloys—a review: PART I—pre-treatment and conversion coating, *Mater. (Basel)* 15 (2022) 8676, <https://doi.org/10.3390/ma15238676>.
- B. Vaghefinazari, E. Wierzbicka, P. Visser, R. Posner, R. Arrabal, E. Matytkina, M. Mojedano, C. Blawert, M.L. Zheludkevich, S.V. Lamaka, Chromate-free corrosion protection strategies for magnesium alloys—a review: Part III—corrosion inhibitors and combining them with other protection strategies, *Mater. (Basel)* 15 (2022) 8489, <https://doi.org/10.3390/ma15238489>.
- E. Wierzbicka, B. Vaghefinazari, M. Mojedano, P. Visser, R. Posner, C. Blawert, M. Zheludkevich, S. Lamaka, E. Matytkina, R. Arrabal, Chromate-free corrosion protection strategies for magnesium alloys—a review: part II—PEO and anodizing, *Mater. (Basel)* 15 (2022) 8515, <https://doi.org/10.3390/ma15238515>.
- B. Bronfin, N. Moscovitch, New magnesium alloys for transmission parts, *Met. Sci. Heat. Treat.* 48 (2006) 479–486, <https://doi.org/10.1007/s11041-006-0121-z>.
- J. Tan, S. Ramakrishna, Applications of magnesium and its alloys: a review, *Appl. Sci.* 11 (2021) 6861, <https://doi.org/10.3390/app11156861>.
- G.L. Song, A. Atrens, Corrosion mechanisms of magnesium alloys, *Adv. Eng. Mater.* 1 (1999) 11–33, [https://doi.org/10.1002/\(SICI\)1527-2648\(199909\)1:1<11::AID-ADEM11>3.0.CO;2-N](https://doi.org/10.1002/(SICI)1527-2648(199909)1:1<11::AID-ADEM11>3.0.CO;2-N).
- Y. Zhang, L. Bourgeois, Y. Chen, Z. Zeng, N. Birbilis, P.N.H. Nakashima, Lithium mapping in a Mg-9Li-4Al-1Zn alloy using electron energy-loss spectroscopy, *J. Magnes. Alloy.* 11 (2023) 1170–1179, <https://doi.org/10.1016/j.jma.2023.03.011>.
- X. Ma, S. Jin, R. Wu, J. Wang, G. Wang, B. Krit, S. Betsofen, Corrosion behavior of Mg–Li alloys: a review, *Trans. Nonferrous Met. Soc. China* 31 (2021) 3228–3254, [https://doi.org/10.1016/S1003-6326\(21\)65728-X](https://doi.org/10.1016/S1003-6326(21)65728-X).
- S. Tang, T. Xin, W. Xu, D. Miskovic, G. Sha, Z. Qadir, S. Ringer, K. Nomoto, N. Birbilis, M. Ferry, Precipitation strengthening in an ultralight magnesium alloy, *Nat. Commun.* 10 (2019), <https://doi.org/10.1038/s41467-019-08954-z>.
- W. Xu, N. Birbilis, G. Sha, Y. Wang, J.E. Daniels, Y. Xiao, M. Ferry, A high-specific-strength and corrosion-resistant magnesium alloy, *Nat. Mater.* 14 (2015) 1229–1235, <https://doi.org/10.1038/nmat4435>.
- R. Islam, M. Haghsheenas, Statistical optimization of stress level in Mg–Li–Al alloys upon hot compression testing, *J. Magnes. Alloy.* 7 (2019) 203–217, <https://doi.org/10.1016/j.jma.2019.03.003>.
- R. Wu, Y. Yan, G. Wang, L.E. Murr, W. Han, Z. Zhang, M. Zhang, Recent progress in magnesium–lithium alloys, *Int. Mater. Rev.* 60 (2015) 65–100, <https://doi.org/10.1179/1743280414Y.0000000044>.
- Y. Zou, L. Zhang, Y. Li, H. Wang, J. Liu, P.K. Liaw, H. Bei, Z. Zhang, Improvement of mechanical behaviors of a superlight Mg–Li base alloy by duplex phases and fine precipitates, *J. Alloy. Compd.* 735 (2018) 2625–2633, <https://doi.org/10.1016/j.jallcom.2017.12.025>.
- C.O. Muga, Z.W. Zhang, Strengthening mechanisms of magnesium–lithium based alloys and composites, *Adv. Mater. Sci. Eng.* 2016 (2016) 1–11, <https://doi.org/10.1155/2016/1078187>.
- C.Q. Li, D.K. Xu, X.-B. Chen, B.J. Wang, R.Z. Wu, E.H. Han, N. Birbilis, Composition and microstructure dependent corrosion behaviour of Mg–Li alloys, *Electrochim. Acta* 260 (2018) 55–64, <https://doi.org/10.1016/j.electacta.2017.11.091>.
- Z. Zhao, Y. Liu, Y. Zhong, X. Chen, Z. Zhang, Corrosion resistance of as-rolled Mg–Li–AlSi Alloys, *Int. J. Electrochem. Sci.* 13 (2018) 4338–4349, <https://doi.org/10.20964/2018.05.16>.
- ASM Specialty Handbook: Magnesium and Magnesium Alloys, ASM INTERNATIONAL, 1999.
- R. Li, B. Jiang, Z. Chen, F. Pan, Z. Gao, Microstructure and mechanical properties of Mg 14Li 1Al 0.3La alloys produced by two-pass extrusion, *J. Rare Earths.* 35 (2017) 1268–1272, <https://doi.org/10.1016/j.jre.2017.08.001>.
- Z. Qu, R. Wu, J. Zhang, M. Zhang, Microstructures and corrosion resistance of three typical superlight Mg–Li alloys, *Int. J. Mater. Res.* 105 (2014) 58–64, <https://doi.org/10.3139/146.110988>.
- D. Xia, Y. Liu, S. Wang, R.C. Zeng, Y. Liu, Y. Zheng, Y. Zhou, In vitro and in vivo investigation on biodegradable Mg–Li–Ca alloys for bone implant application, *Sci. China Mater.* 62 (2019) 256–272, <https://doi.org/10.1007/s40843-018-9293-8>.
- J. Wu, D. Zhao, J.M. Ohodnicki, B. Lee, A. Roy, R. Yao, S. Chen, Z. Dong, W. R. Heineman, P.N. Kumta, In vitro and in vivo evaluation of multiphase ultrahigh ductility Mg–Li–Zn alloys for cardiovascular stent application, *ACS Biomater. Sci. Eng.* 4 (2018) 919–932, <https://doi.org/10.1021/acsbomaterials.7b00854>.
- R. Wang, Q. Li, N. Wang, C. Peng, Y. Feng, Effect of lithium on the discharge and corrosion behavior of Mg-3 wt% Al alloy as the anode for seawater activated battery, *J. Mater. Eng. Perform.* 27 (2018) 6552–6563, <https://doi.org/10.1007/s11665-018-3750-7>.
- X. Zong, J. Zhang, W. Liu, J. Chen, K. Nie, C. Xu, Effects of Li on microstructures, mechanical, and biocorrosion properties of biodegradable Mg 94-x Zn 2 Y 4 Li x alloys with long period stacking ordered phase, *Adv. Eng. Mater.* 19 (2017) 1600606, <https://doi.org/10.1002/adem.201600606>.
- G. Tian, J. Wang, S. Wang, C. Xue, X. Yang, H. Su, An ultra-light Mg–Li alloy with exceptional elastic modulus, high strength, and corrosion-resistance, *Mater. Today Commun.* 35 (2023) 105623, <https://doi.org/10.1016/j.matcomm.2023.105623>.
- T.W. Cain, J.P. Labukas, The development of  $\beta$  phase Mg–Li alloys for ultralight corrosion resistant applications, *Npj Mater. Degrad.* 4 (2020) 17, <https://doi.org/10.1038/s41529-020-0121-2>.
- D.S. Kharitonov, M. Zimowska, J. Ryl, A. Zieliński, M.A. Osipenko, J. Adamiec, A. Wrzesińska, P.M. Claesson, I.I. Kurilo, Aqueous molybdate provides effective corrosion inhibition of WE43 magnesium alloy in sodium chloride solutions, *Corros. Sci.* 190 (2021) 109664, <https://doi.org/10.1016/j.corsci.2021.109664>.
- Z. Hu, Z. Yin, Z. Yin, K. Wang, Q. Liu, P. Sun, H. Yan, H. Song, C. Luo, H. Guan, C. Luc, Corrosion behavior characterization of as extruded Mg-8Li-3Al alloy with minor alloying elements (Gd, Sn and Cu) by scanning Kelvin probe force microscopy, *Corros. Sci.* 176 (2020) 108923, <https://doi.org/10.1016/j.corsci.2020.108923>.
- Z. Zeng, M. Zhou, M. Esmaily, Y. Zhu, S. Choudhary, J.C. Griffith, J. Ma, Y. Hora, Y. Chen, A. Gullino, Q. Shi, H. Fujii, N. Birbilis, Corrosion resistant and high-

- strength dual-phase Mg-Li-Al-Zn alloy by friction stir processing, *Commun. Mater.* 3 (2022) 18, <https://doi.org/10.1038/s43246-022-00245-3>.
- [37] T. Morishige, Y. Obata, T. Goto, T. Fukagawa, E. Nakamura, T. Takenaka, Effect of Al composition on the corrosion resistance of Mg-14 mass% Li system alloy, *Mater. Trans.* 57 (2016) 1853–1856, <https://doi.org/10.2320/matertrans.M2016247>.
- [38] Y. Song, D. Shan, R. Chen, E.-H. Han, Corrosion characterization of Mg–8Li alloy in NaCl solution, *Corros. Sci.* 51 (2009) 1087–1094, <https://doi.org/10.1016/j.corsci.2009.03.011>.
- [39] Z.-Y. Ding, L.-Y. Cui, R.-C. Zeng, Y.-B. Zhao, S.-K. Guan, D.-K. Xu, C.-G. Lin, Exfoliation corrosion of extruded Mg-Li-Ca alloy, *J. Mater. Sci. Technol.* 34 (2018) 1550–1557, <https://doi.org/10.1016/j.jmst.2018.05.014>.
- [40] B. Zaghoul, C.F. Glover, J.R. Scully, J.R. Kish, Inhibiting corrosion of Mg Alloy AZ31B-H24 sheet metal with lithium carbonate, *Corrosion* 77 (2021) 192–203, <https://doi.org/10.5006/3625>.
- [41] D.S. Kharitonov, J. Sommertune, C. Örnek, J. Ryl, I.I. Kurilo, P.M. Claesson, J. Pan, Corrosion inhibition of aluminium alloy AA6063-T5 by vanadates: local surface chemical events elucidated by confocal Raman micro-spectroscopy, *Corros. Sci.* 148 (2019) 237–250, <https://doi.org/10.1016/j.corsci.2018.12.011>.
- [42] D.S. Kharitonov, I. Dobryden, B. Sefer, J. Ryl, A. Wrzesińska, I.V. Makarova, I. Bobowska, I.I. Kurilo, P.M. Claesson, Surface and corrosion properties of AA6063-T5 aluminum alloy in molybdate-containing sodium chloride solutions, *Corros. Sci.* 171 (2020) 108658, <https://doi.org/10.1016/j.corsci.2020.108658>.
- [43] S.V. Lamaka, B. Vaghefinazari, D. Mei, R.P. Petruskas, D. Höche, M. L. Zheludkevich, Comprehensive screening of Mg corrosion inhibitors, *Corros. Sci.* 128 (2017) 224–240, <https://doi.org/10.1016/j.corsci.2017.07.011>.
- [44] M.A. Osipenko, D.S. Kharytonau, A.A. Kasach, J. Ryl, J. Adamiec, I.I. Kurilo, Inhibitive effect of sodium molybdate on corrosion of AZ31 magnesium alloy in chloride solutions, *Electrochim. Acta* 414 (2022) 140175, <https://doi.org/10.1016/j.electacta.2022.140175>.
- [45] M.A. Osipenko, A.A. Kasach, J. Adamiec, M. Zimowska, I.I. Kurilo, D. S. Kharytonau, Corrosion inhibition of magnesium alloy AZ31 in chloride-containing solutions by aqueous permanganate, *J. Solid State Electrochem.* (2023), <https://doi.org/10.1007/s10008-023-05472-3>.
- [46] S. Tang, T. Xin, W. Xu, D. Miskovic, C. Li, N. Birbilis, M. Ferry, The composition-dependent oxidation film formation in Mg-Li-Al alloys, *Corros. Sci.* 187 (2021) 109508, <https://doi.org/10.1016/j.corsci.2021.109508>.
- [47] Y.M. Yan, A. Maltseva, P. Zhou, X.J. Li, Z.R. Zeng, O. Gharbi, K. Ogle, M. La Haye, M. Vaudesca, M. Esmaily, N. Birbilis, P. Volovitch, On the in-situ aqueous stability of an Mg-Li-(Al-Y-Zr) alloy: Role of Li, *Corros. Sci.* 164 (2020) 108342, <https://doi.org/10.1016/j.corsci.2019.108342>.
- [48] Y. Yan, Y. Qiu, O. Gharbi, N. Birbilis, P.N.H. Nakashima, Characterisation of Li in the surface film of a corrosion resistant Mg-Li-(Al-Y-Zr) alloy, *Appl. Surf. Sci.* 494 (2019) 1066–1071, <https://doi.org/10.1016/j.apsusc.2019.07.167>.
- [49] M.A. Osipenko, J. Karczewski, M. Dominów, M. Przeźniak-Welenc, I.V. Makarava, I. Kurilo, D.S. Kharytonau, J. Ryl, Multisite impedimetric monitoring with an in-depth distribution of relaxation times analysis of WE43 and AZ31 magnesium alloys corrosion, *Measurement* 222 (2023) 113683, <https://doi.org/10.1016/j.measurement.2023.113683>.
- [50] M.A. Osipenko, J. Karczewski, M. Dominów, M. Przeźniak-Welenc, J. Gurgul, I. I. Kurilo, J. Ryl, D.S. Kharytonau, Exploring mechanism of corrosion inhibition of WE43 and AZ31 alloys by aqueous molybdate in Hank's solution by multisite impedimetric monitoring, *Corros. Sci.* (2024) 111979, <https://doi.org/10.1016/j.corsci.2024.111979>.
- [51] J. Wysocka, S. Krakowiak, J. Ryl, Evaluation of citric acid corrosion inhibition efficiency and passivation kinetics for aluminium alloys in alkaline media by means of dynamic impedance monitoring, *Electrochim. Acta* 258 (2017) 1463–1475, <https://doi.org/10.1016/j.electacta.2017.12.017>.
- [52] J. Ryl, J. Wysocka, M. Cieslik, H. Gerengi, T. Ossowski, S. Krakowiak, P. Niedzialkowski, Understanding the origin of high corrosion inhibition efficiency of bee products towards aluminium alloys in alkaline environments, *Electrochim. Acta* 304 (2019) 263–274, <https://doi.org/10.1016/j.electacta.2019.03.012>.
- [53] J. Wysocka, S. Krakowiak, J. Ryl, K. Darowicki, Investigation of the electrochemical behaviour of AA1050 aluminium alloy in aqueous alkaline solutions using Dynamic Electrochemical Impedance Spectroscopy, *J. Electroanal. Chem.* 778 (2016) 126–136, <https://doi.org/10.1016/j.jelechem.2016.08.028>.
- [54] D.S. Kharitonov, C. Ornek, P.M. Claesson, J. Sommertune, I.M. Zharskii, I.I. Kurilo, J. Pan, Corrosion inhibition of aluminum alloy AA6063-T5 by vanadates: microstructure characterization and corrosion analysis, *J. Electrochem. Soc.* 165 (2018) C116–C126, <https://doi.org/10.1149/2.0341803jes>.
- [55] F. Gao, L. Han, Implementing the Nelder-Mead simplex algorithm with adaptive parameters, *Comput. Optim. Appl.* 51 (2012) 259–277, <https://doi.org/10.1007/s10589-010-9329-3>.
- [56] N.P. Papenberg, S. Gneiger, I. Weisensteiner, P.J. Uggowitzer, S. Pogatscher, Mg-alloys for forging applications—a review, *Mater. (Basel)* 13 (2020) 985, <https://doi.org/10.3390/ma13040985>.
- [57] R. Maurya, D. Mittal, K. Balani, Effect of heat-treatment on microstructure, mechanical and tribological properties of Mg-Li-Al based alloy, *J. Mater. Res. Technol.* 9 (2020) 4749–4762, <https://doi.org/10.1016/j.jmrt.2020.02.101>.
- [58] G. Tian, J. Wang, C. Xue, S. Wang, X. Yang, H. Su, Q. Li, X. Li, C. Yan, Z. Yang, Improving corrosion resistance of Mg-Li alloys by Sn microalloying, *J. Mater. Res. Technol.* 26 (2023) 199–217, <https://doi.org/10.1016/j.jmrt.2023.07.205>.
- [59] G. Tian, J. Wang, C. Zhang, H. Su, C. Yan, Z. Yang, Quantifying the influence of microstructure on the corrosion of Mg-Li alloys by using X-ray CT, *Corros. Sci.* 229 (2024) 111848, <https://doi.org/10.1016/j.corsci.2024.111848>.
- [60] J. Xie, Y. Zhou, C. Zhou, X. Li, Y. Chen, Microstructure and mechanical properties of Mg–Li alloys fabricated by wire arc additive manufacturing, *J. Mater. Res. Technol.* 29 (2024) 3487–3493, <https://doi.org/10.1016/j.jmrt.2024.02.094>.
- [61] A.V. Paspelau, A.A. Kasach, J. Gurgul, G. Mordarski, K. Skowron, I.I. Kurilo, D. S. Kharytonau, Deposition and corrosion performance of phosphate-poly(lactic acid) composite coatings on WE43 magnesium alloy, *Surf. Coat. Technol.* 478 (2024) 130419, <https://doi.org/10.1016/j.surfcoat.2024.130419>.
- [62] N. Birbilis, A.D. King, S. Thomas, G.S. Frankel, J.R. Scully, Evidence for enhanced catalytic activity of magnesium arising from anodic dissolution, *Electrochim. Acta* 132 (2014) 277–283, <https://doi.org/10.1016/j.electacta.2014.03.133>.
- [63] L.G. Bland, A.D. King, N. Birbilis, J.R. Scully, Assessing the corrosion of commercially pure magnesium and commercial AZ31B by electrochemical impedance, mass-loss, hydrogen collection, and inductively coupled plasma optical emission spectrometry solution analysis, *Corrosion* 71 (2015) 128–145, <https://doi.org/10.5006/1419>.
- [64] Z. Feng, B. Hurley, M. Zhu, Z. Yang, J. Hwang, R. Buchheit, Corrosion Inhibition of AZ31 Mg Alloy by Aqueous Selenite (SeO<sub>3</sub><sup>2-</sup>), *J. Electrochem. Soc.* 166 (2019) C520–C529, <https://doi.org/10.1149/2.0911914jes>.
- [65] Y. Song, D. Shan, R. Chen, E.H. Han, Corrosion characterization of Mg-8Li alloy in NaCl solution, *Corros. Sci.* 51 (2009) 1087–1094, <https://doi.org/10.1016/j.corsci.2009.03.011>.
- [66] A.D. King, N. Birbilis, J.R. Scully, Accurate electrochemical measurement of magnesium corrosion rates; A combined impedance, mass-loss and hydrogen collection study, *Electrochim. Acta* 121 (2014) 394–406, <https://doi.org/10.1016/j.electacta.2013.12.124>.
- [67] A. Soltan, M.S. Dargusch, Z. Shi, D. Gerrard, S. Al Shabibi, Y. Kuo, A. Atrens, Corrosion of Mg alloys EV31A, WE43B, and ZE41A in chloride- and sulfate-containing solutions saturated with magnesium hydroxide, *Mater. Corros.* 71 (2020) 956–979, <https://doi.org/10.1002/maco.201911375>.
- [68] L. Wang, D. Snihirova, M.D. Havigh, M. Deng, S.V. Lamaka, H. Terryn, M. L. Zheludkevich, Non-stationarity in electrochemical impedance measurement of Mg-based materials in aqueous media, *Electrochim. Acta* 468 (2023) 143140, <https://doi.org/10.1016/j.electacta.2023.143140>.
- [69] J. Orlikowski, J. Ryl, M. Jarzynka, S. Krakowiak, K. Darowicki, Instantaneous impedance monitoring of aluminum alloy 7075 corrosion in borate buffer with admixed chloride ions, *Corrosion* 71 (2015) 828–838, <https://doi.org/10.5006/1546>.
- [70] L. Wang, D. Snihirova, M. Deng, C. Wang, B. Vaghefinazari, G. Wiese, M. Langridge, D. Höche, S.V. Lamaka, M.L. Zheludkevich, Insight into physical interpretation of high frequency time constant in electrochemical impedance spectra of Mg, *Corros. Sci.* 187 (2021) 109501, <https://doi.org/10.1016/j.corsci.2021.109501>.
- [71] M. Deng, D. Höche, S.V. Lamaka, D. Snihirova, M.L. Zheludkevich, Mg-Ca binary alloys as anodes for primary Mg-air batteries, *J. Power Sources* 396 (2018) 109–118, <https://doi.org/10.1016/j.jpowsour.2018.05.090>.
- [72] Y. Li, X. Lu, K. Wu, L. Yang, T. Zhang, F. Wang, Exploration the inhibition mechanism of sodium dodecyl sulfate on Mg alloy, *Corros. Sci.* 168 (2020) 108559, <https://doi.org/10.1016/j.corsci.2020.108559>.
- [73] C. Song, C. Wang, D. Mercier, B. Vaghefinazari, A. Seyeux, D. Snihirova, D.C. F. Wieland, P. Marcus, M.L. Zheludkevich, S.V. Lamaka, Corrosion inhibition mechanism of 2,6-pyridinedicarboxylate depending on magnesium surface treatment, *Corros. Sci.* 229 (2024) 111867, <https://doi.org/10.1016/j.corsci.2024.111867>.
- [74] B. Hirschorn, M.E. Orazem, B. Tribollet, V. Vivier, I. Frateur, M. Musiani, Determination of effective capacitance and film thickness from constant-phase-element parameters, *Electrochim. Acta* 55 (2010) 6218–6227, <https://doi.org/10.1016/j.electacta.2009.10.065>.
- [75] S. Thomas, N.V. Medhekar, G.S. Frankel, N. Birbilis, Corrosion mechanism and hydrogen evolution on Mg, *Curr. Opin. Solid State Mater. Sci.* 19 (2015) 85–94, <https://doi.org/10.1016/j.cossms.2014.09.005>.
- [76] A. Maltseva, V. Shkirskiy, G. Lefèvre, P. Volovitch, Effect of pH on Mg(OH)<sub>2</sub> film evolution on corroding Mg by in situ kinetic Raman mapping (KRM), *Corros. Sci.* 153 (2019) 272–282, <https://doi.org/10.1016/j.corsci.2019.03.024>.
- [77] A. Maltseva, S.V. Lamaka, K.A. Yasakau, D. Mei, D. Kurchavov, M.L. Zheludkevich, G. Lefèvre, P. Volovitch, In situ surface film evolution during Mg aqueous corrosion in presence of selected carboxylates, *Corros. Sci.* 171 (2020) 108484, <https://doi.org/10.1016/j.corsci.2020.108484>.
- [78] P. Dawson, C.D. Hadfield, G.R. Wilkinson, The polarized infra-red and Raman spectra of Mg(OH)<sub>2</sub> and Ca(OH)<sub>2</sub>, *J. Phys. Chem. Solids* 34 (1973) 1217–1225, [https://doi.org/10.1016/S0022-3697\(73\)80212-4](https://doi.org/10.1016/S0022-3697(73)80212-4).
- [79] V. Prigobbe, Estimation of nucleation and growth parameters from in situ Raman spectroscopy in carbonate systems, *J. Environ. Chem. Eng.* 6 (2018) 930–936, <https://doi.org/10.1016/j.jece.2017.12.024>.
- [80] P. Pasierb, S. Komornicki, M. Rokita, M. Rękas, Structural properties of Li<sub>2</sub>CO<sub>3</sub>-BaCO<sub>3</sub> system derived from IR and Raman spectroscopy, *J. Mol. Struct.* 596 (2001) 151–156, [https://doi.org/10.1016/S0022-2860\(01\)00703-7](https://doi.org/10.1016/S0022-2860(01)00703-7).
- [81] K.-H. Tytko, *Gmelin Handbook of Inorganic Chemistry. Mo Molybdenum* (Berlin Heidelberg), Springer, Berlin, Heidelberg, 1986, <https://doi.org/10.1007/978-3-662-08837-1>.
- [82] P.A. Spevack, N.S. McIntyre, A Raman and XPS investigation of supported molybdenum oxide thin films. 1. Calcination and reduction studies, *J. Phys. Chem.* 97 (1993) 11020–11030, <https://doi.org/10.1021/j100144a020>.
- [83] M.A. Camacho-López, L. Escobar-Alarcón, M. Picquart, R. Arroyo, G. Córdoba, E. Haro-Poniatowski, Micro-Raman study of the m-MoO<sub>2</sub> to α-MoO<sub>3</sub> transformation induced by cw-laser irradiation, *Opt. Mater. (Amst.)* 33 (2011) 480–484, <https://doi.org/10.1016/j.optmat.2010.10.028>.

- [84] M. Dieterle, G. Mestl, Raman spectroscopy of molybdenum oxides: part II. Resonance Raman spectroscopic characterization of the molybdenum oxides Mo<sub>4</sub>O<sub>11</sub> and MoO<sub>2</sub>, *Phys. Chem. Chem. Phys.* 4 (2002) 822–826, <https://doi.org/10.1039/b107046k>.
- [85] E. Payen, J. Grimblot, S. Kasztelan, Study of oxidic and reduced alumina-supported molybdate and heptamolybdate species by in situ laser Raman spectroscopy, *J. Phys. Chem.* 91 (1987) 6642–6648, <https://doi.org/10.1021/j100311a018>.
- [86] H. Verbruggen, K. Baert, H. Terryn, I. De Graeve, Molybdate-phosphate conversion coatings to protect steel in a simulated concrete pore solution, *Surf. Coat. Technol.* 361 (2019) 280–291, <https://doi.org/10.1016/j.surfcoat.2018.09.056>.
- [87] M. Wang, J. You, A.A. Sobol, J. Wang, J. Wu, X. Lv, Temperature-dependent Raman spectroscopic studies of microstructure present in dipotassium molybdate crystals and their melts, *J. Raman Spectrosc.* 47 (2016) 1259–1265, <https://doi.org/10.1002/jrs.4948>.
- [88] B. Botar, A. Ellern, P. Kögerler, Mapping the formation areas of giant molybdenum blue clusters: A spectroscopic study, *Dalt. Trans.* 41 (2012) 8951–8959, <https://doi.org/10.1039/c2dt30661a>.
- [89] M.L. Xanes, H. Hu, I.E. Wachs, A. Drive, S.R. Bare, Surface structures of supported molybdenum oxide catalysts, *Characterization* (1995) 10897–10910.
- [90] Y. Yao, B. Gao, J. Chen, L. Yang, Engineered biochar reclaiming phosphate from aqueous solutions: mechanisms and potential application as a slow-release fertilizer, *Environ. Sci. Technol.* 47 (2013) 8700–8708, <https://doi.org/10.1021/es4012977>.
- [91] A.I. Ikeuba, B. Zhang, J. Wang, E.-H. Han, W. Ke, P.C. Okafor, SVET and SIET Study of galvanic corrosion of Al/MgZn 2 in aqueous solutions at different pH, *J. Electrochem. Soc.* 165 (2018) C180–C194, <https://doi.org/10.1149/2.0861803jes>.
- [92] J. Baltrusaitis, B. Mendoza-Sanchez, V. Fernandez, R. Veenstra, N. Dukstiene, A. Roberts, N. Fairley, Generalized molybdenum oxide surface chemical state XPS determination via informed amorphous sample model, *Appl. Surf. Sci.* 326 (2015) 151–161, <https://doi.org/10.1016/j.apsusc.2014.11.077>.